TITLE

Cryo-EM structures of a LRRC8 chimera with native functional properties reveal heptameric assembly

AUTHORS

Hirohide Takahashi[1,2], Toshiki Yamada[3], Jerod S. Denton[3,4], Kevin Strange[3], Erkan Karakas[1,2,*]

[1] Department of Molecular Physiology and Biophysics, Vanderbilt University, School of Medicine, Nashville, TN, 37232, USA.

[2] Center for Structural Biology, Vanderbilt University; Nashville, TN, 37232, USA.

[3] Department of Anesthesiology, Vanderbilt University Medical Center, Nashville, TN, 37232, USA.

[4] Department of Pharmacology, Vanderbilt University, School of Medicine, Nashville, TN, 37232, USA.

[*] Corresponding author. erkan.karakas@vanderbilt.edu

ABSTRACT

Volume-regulated anion channels (VRACs) mediate volume regulatory Cl^- and organic solute efflux from vertebrate cells. VRACs are heteromeric assemblies of LRRC8A-E proteins with unknown stoichiometries. Homomeric LRRC8A and LRRC8D channels have a small pore, hexameric structure. However, these channels are either non-functional nor exhibit abnormal regulation and pharmacology, limiting their utility for structure-function analyses. We circumvented these limitations by developing novel homomeric LRRC8 chimeric channels with functional properties consistent with those of native VRAC/LRRC8 channels. We demonstrate here that the LRRC8C-LRRC8A($IL1^{25}$) chimera comprising LRRC8C and 25 amino acids unique to the first intracellular loop (IL1) of LRRC8A has a heptameric structure like that of homologous pannexin channels. Unlike homomeric LRRC8A and LRRC8D channels, heptameric LRRC8C-LRRC8A($IL1^{25}$) channels have a large-diameter pore similar to that estimated for native VRACs, exhibit normal DCPIB pharmacology, and have higher permeability to large organic anions. Lipid-like densities are located between LRRC8C-LRRC8A($IL1^{25}$) subunits and occlude the channel pore. Our findings provide new insights into VRAC/LRRC8 channel structure and suggest that lipids may play important roles in channel gating and regulation.

INTRODUCTION

Volume Regulated Anion Channels, VRACs, are expressed widely in vertebrate cell types where they mediate the efflux of Cl^- and organic solutes required for cell volume regulation (Jentsch, 2016a; Jentsch, 2016b; Strange et al., 2019). VRACs are activated by increases in cell volume and by large reductions in intracellular ionic strength (Strange et al., 2019).

VRACs are encoded by the *Lrrc8* gene family (Qiu et al., 2014; Voss et al., 2014), which comprises five paralogs termed *Lrrc8a-e* (Abascal & Zardoya, 2012; Voss et al., 2014). Native VRAC/LRRC8 channels are heteromers with unknown stoichiometry. LRRC8A is an essential VRAC/LRRC8 subunit and must be co-expressed with at least one other paralog to reconstitute volume-regulated channel activity (Syeda et al., 2016; Voss et al., 2014). High resolution cryo-EM structures have been determined for homomeric LRRC8A (Deneka et al., 2021; Deneka et al., 2018; Kasuya et al., 2018; Kefauver et al., 2018; Kern et al., 2019) and LRRC8D (Nakamura et al., 2020) channels demonstrating that they have a hexameric configuration.

Defining the molecular basis by which VRAC and other volume-sensitive channels detect cell volume changes is a fundamental and longstanding physiological problem. Detailed molecular understanding of this important problem requires accurate channel structural information. Homomeric LRRC8A and LRRC8D channels have abnormal functional properties or are not expressed in the plasma cell membrane (Voss et al., 2014; Yamada et al., 2021b; Yamada & Strange, 2018; Zhou et al., 2018). Structure-function studies of VRAC/LRRC8 heteromeric channels are complicated by their undefined, likely variable, and experimentally uncontrollable stoichiometry. To circumvent these problems, we developed a series of novel homomeric LRRC8 chimeras that exhibit functional properties similar to the native heteromeric VRAC/LRRC8 channels (Yamada & Strange, 2018).

We describe here the cryo-electron microscopy structures of the LRRC8C-LRRC8A($IL1^{25}$) chimera, hereafter termed 8C-8A($IL1^{25}$). 8C-8A($IL1^{25}$) consists of a 25-amino acid sequence unique to the first intracellular loop, IL1, of LRRC8A inserted into the

corresponding region of LRRC8C (Fig. 1). Like native VRAC/LRRC8 channels, 8C-8A(IL1^{25}) chimeras are activated strongly by cell swelling and low intracellular ionic strength (Yamada & Strange, 2018). We demonstrate that the 8C-8A(IL1^{25}) chimeric channel is a large-pore 7-subunit heptamer, like homologous pannexin channels (Bhat & Sajjad, 2021; Deng et al., 2020; Jin et al., 2020; Kuzuya et al., 2022; Michalski et al., 2020; Mou et al., 2020; Qu et al., 2020; Ruan et al., 2020). The pore diameter is similar to that estimated for native VRACs, and permeability to large organic anions is significantly higher than that of homohexameric LRRC8A channels. Lipid-like densities are located between 8C-8A(IL1^{25}) channel subunits and occlude the channel pore, as has been shown recently for human pannexin 1 (Kuzuya et al., 2022). Our results, together with the previous studies (Deneka et al., 2021; Deneka et al., 2018; Kasuya et al., 2018; Kefauver et al., 2018; Kern et al., 2019; Nakamura et al., 2020), demonstrate that LRRC8 proteins can form anion channels with different subunit numbers.

RESULTS

Structure determination

To facilitate structure-function understanding of VRAC/LRRC8 channel regulation and pore properties, we expressed the 8C-8A(IL1^{25}) chimera in Sf9 insect cells and purified the detergent-solubilized complexes by affinity and size exclusion chromatography (Fig. 1–figure supplement 1). The purified 8C-8A(IL1^{25}) complex appeared larger than the LRRC8A hexamers in both native-PAGE and size exclusion chromatography analysis (Fig. 1–figure supplement 1B-C). We performed single-particle cryo-EM analysis to determine the structure of the complex (Fig. 2 and Fig. 2–figure supplement 1 and 2). Following 2D classification and ab initio 3D reconstruction, we performed 3D classification and obtained five distinct 3D classes for 8C-8A(IL1^{25}) (Fig. 2–figure supplement 1). The 8C-8A(IL1^{25}) maps showed no apparent symmetric arrangement. Therefore, the final reconstructions were done without enforcing any symmetry

and resulted in five structures with resolutions in the range of 3.3 to 4.0 Å (Figs. 2A, B, Fig. 2–figure supplement 1 and 2, and Table 1).

Similar to LRRC8A and LRRC8D structures, the 8C-8A(IL1^{25}) structure comprises four domains, the extracellular domain (ECD), transmembrane domain (TMD), intracellular domain (ICD), and leucine-rich repeat (LRR) motif-containing domain (LRRD) (Fig. 2). The cryo-EM maps for the ECD and TMD revealed high resolution features allowing us to build an atomic model comprising most of the ECD and TMD except residues 60-94 in the ECD and the first 15 residues of the N-terminus. The quality of the cryo-EM maps for the ICDs was improved by performing local refinements, and the resulting maps were used to build a model (Fig. 2–figure supplement 2). However, the first intracellular loop containing the swapped IL1^{25} region remained unresolved. Although the unsharpened maps revealed clear features for the entire protein, the local resolution for the LRRD was insufficient to build an atomic model, and the local refinement strategy we applied did not provide any meaningful improvement in LRRD resolution (Fig 2A-E and Fig. 2–figure supplement 1 and 2). Therefore, we did not build an atomic model for the LRRD and used the maps without B-factor sharpening to assess their structure and overall arrangement relative to the rest of the protein complex (Fig. 2D-E).

8C-8A(IL1^{25}) chimeras form heptameric channels

The overall structure of an individual 8C-8A(IL1^{25}) subunit is similar to that of LRRC8A (Fig. 2F) and LRRC8D. However, unlike homomeric LRRC8A and LRRC8D channels, which are hexamers (Deneka et al., 2021; Deneka et al., 2018; Kasuya et al., 2018; Kefauver et al., 2018; Kern et al., 2019; Nakamura et al., 2020), the 8C-8A(IL1^{25}) chimeric channel is a 7 subunit heptamer, similar to the homologous pannexin channels (Figs. 2B and 2E; Fig. 2–figure supplement 3) (Bhat & Sajjad, 2021; Deng et al., 2020; Jin et al., 2020; Kuzuya et al., 2022; Michalski et al., 2020; Mou et al., 2020; Qu et al., 2020; Ruan et al., 2020).

The subunit arrangement of the 8C-8A(IL1^{25}) heptameric channel is asymmetric as opposed to LRRC8A and LRRC8D hexamers, which have 2-, 3-, or 6-fold symmetric arrangements (Deneka et al., 2021; Deneka et al., 2018; Kasuya et al., 2018; Kefauver et al., 2018; Kern et al., 2019; Nakamura et al., 2020). When the ICD and TMD are viewed from the cytoplasm, 8C-8A(IL1^{25}) subunits are organized into two distinct groups, one with four subunits and the other with three subunits (Fig. 3A-D). These two groups of subunits associate via a loose interface, while the subunits within each group associate via a tight interface (Fig. 3A-D and Fig. 3–figure supplement 1-3).

In contrast to the ICDs and TMDs, the ECDs are arranged symmetrically and form extensive contacts between the subunits in both tight and loose interfaces (Fig. 3E and Fig. 3–figure supplement 1). Most of the subunit interaction is between the residues on ELH1 and the linker that connects EL2β1 and EL2β2 in one subunit and the residues on the three β-strands of the neighboring subunit (Fig. 3E and Fig. 3–figure supplement 1). The contacts between each subunit pair bury about 1,900 Å^2 of solvent-accessible surface area at the ECDs (Table 2). The buried solvent-accessible surface areas between the subunit pairs in the TMDs and ICDs are considerably smaller and exhibit high variability between the tight and the loose interfaces. In the TMD, the buried areas are about 650 Å^2 and 110 Å^2 for the tight and loose interfaces, respectively (Table 2). The residues within the core of the TMD are loosely associated and the major interactions of the subunits within the TMD are mediated by the residues closer to the ECDs or ICDs at the tight interface (Fig. 3–figure supplement 2). At the loose interface, only residues closer to the ECD are in close range for direct interaction (Fig. 3–figure supplement 2). In the ICD, the buried areas in the tight interfaces range from 290 to 560 Å^2, whereas there are no solvent-inaccessible contacts at the loose interfaces (Fig. 3E, Fig. 3–figure supplement 2-3, and Table 2).

The asymmetric arrangement observed for the TMDs and ICDs is likely due to their divergent orientation relative to the ECDs. Figure 4A shows the alignment of the seven subunits

on their ECDs. TMDs do not align and exhibit up to an 8° difference in their orientation relative to the ECD, while the difference is larger for the ICDs (Fig. 4A). Another notable difference between the subunits is in the linker that connects the first β-strand on extracellular loop 1, EL1β1, of the ECD to the transmembrane helix 1 (TM1) of the TMD (Fig. 4A-B). In two of the subunits in the class 1 structure, K51 points toward the pore, while D50 points in the opposite direction. In the five other subunits, D50 points toward the pore, and K51 is oriented toward the subunit interface (Fig. 4C). When K51 points toward the pore, it creates a groove between the subunits (Fig. 4D). These grooves, located between the subunits forming the loose interface in the class 1 structure, connect the space within the ECD to the membrane-facing surface of the TMD (Fig 4E). When D50 points toward the pore, the side chain of K51 occupies this space, closing the groove (Fig. 4F).

Structural heterogeneity of 8C-8A(IL1^{25}) chimeras

We obtained five distinct 3D classes for the 8C-8A(IL1^{25}) chimera. The most apparent difference between the structures is in the arrangement of the LRRDs (Fig. 5A-B). In class 1, all seven LRRDs are arranged circularly with roughly 7-fold symmetry. For class 5, one of the LRRDs is positioned outside of the quaternary assembly formed by six LRRDs arranged with pseudo-2-fold symmetry. The density for the LRRD located outside the assembly is poorly visible, indicating high flexibility relative to the rest of the complex (Fig. 5A-B). The arrangements of the LRRDs in the other three 3D classes exhibit diverse arrangements and subunit interactions. As a result, several different subunit interfaces exist between the neighboring LRRDs. However, a detailed analysis of these interfaces is not possible due to the limited resolution of the cryo-EM maps for these regions, prohibiting the building of the models with amino acid assignments.

Consistent with the conformational differences in the arrangements of the LRRDs, the ICDs also exhibit conformational heterogeneity, albeit less pronounced, among the five 3D classes we observed (Fig. 5C and Fig. 5–figure supplement 1). Fig. 5C shows the arrangement

of the ICDs and the distances between the Cα atoms of G163 of the neighboring subunits. The non-symmetric and diverse subunit arrangement is evident. The distances between the subunits forming the tight interfaces appear similar in all classes, whereas the distances between the subunits forming the loose interfaces are variable among different classes. A similar variation is also observed within the TMD (Fig. 5D and Fig. 5–figure supplement 1). However, there are no apparent structural differences at the ECD of the structures (Fig. 5–figure supplement 1).

The distinct arrangement of the loops formed by D50 and K51 is also observed in other classes (Fig. 5–figure supplement 2). However, the number of subunits with K51 pointing toward the pores differs. For example, the class 2 structure has only one subunit with K51 pointing toward the pore, compared to 2 subunits in the class 1 structure (Fig. 5–figure supplement 2). The groove created by the distinct K51 arrangement is located between the subunits that form one of the two loose interfaces in the class 2 structure, despite the presence of two loose interfaces. It is plausible that this loop is flexible and adopts distinct conformations, possibly depending on the orientation of the TMD relative to the ECD. However, it is not clear if there is any direct correlation between the K51 orientation and the loose interfaces.

Pore structure

Figure 6 shows the pore domain of the 8C-8A(IL1^{25}) heptameric chimera compared to the pore domain of LRRC8A hexameric channels. The narrowest region of the heptameric 8C-8A(IL1^{25}) channel pore has an average solvent-accessible radius of 4.7 Å and is formed by L105 located on the extracellular side of the protein (Fig. 6A). This is considerably larger than the pore radius of 2.0 Å determined from cryo-EM structures of hexameric LRRC8A channels (Fig. 6B-C) (Deneka et al., 2018; Kasuya et al., 2018; Kefauver et al., 2018; Kern et al., 2019).

The difference in pore diameters of hexameric LRRC8A channels and heptameric 8C-8A(IL1^{25}) channels implies that subunit number impacts channel solute permeability. To assess this directly, we quantified the relative permeabilities (i.e., P_x/P_{Cl}) of LRRC8A and 8C-8A(IL1^{25})

to the large organic anions glutathione and lactobionate. $P_{glutathione}/P_{Cl}$ and $P_{lactobionate}/P_{Cl}$ were both significantly ($P<0.01$) higher for the 8C-8A($IL1^{25}$) heptameric channel (Fig. 6D-E), consistent with its larger pore diameter.

Interaction of lipids with the 8C-8A($IL1^{25}$)

As shown in Fig. 7A, we observe non-protein densities penetrating through the openings between the subunits in the TMD. The shape and length of these densities are consistent with lipid molecules. Similar densities are observed in LRRC8A hexameric channels reconstituted in lipid nanodiscs (Kern et al., 2019). We observe these lipid-like densities on both the cytoplasmic and extracellular sides of the TMD. The lipid-like densities on the extracellular side do not show apparent differences between tight and loose interfaces. However, the lipid-like density closer to the intracellular side is considerably weaker at the loose interfaces compared to the ones at the tight interfaces (Fig. 7A). This difference may be due to the larger separation of the subunits at the loose interface, creating more room for the lipid molecules to move.

Although the quality of the maps does not allow us to identify the lipid molecules leading to the densities we observe, the ones with the strongest features suggest phospholipids as the most likely candidates (Fig. 7B). As shown in Fig. 7B, a phospholipid molecule can be reasonably fitted into the strongest density we observe. The polar phosphate moiety of the lipid molecule is coordinated by two lysine residues (K125 and K318) and a histidine residue (H314) of the neighboring subunits (Fig. 7B). W122, Y126, and L130 are close to the acyl chains (Fig. 7B). One of the acyl chains extends through the space between the subunit and reaches the interior surface of the channel. The second acyl chain is less defined. The area contains additional non-protein densities suggesting the presence of other ordered lipid molecules.

When we examined the surface properties of the pore lining residues, we found high densities of charged amino acid residues that align with the phospholipid head groups of the

membrane bilayer surrounding the TMD (Fig 7C). A hydrophobic patch of amino acid residues aligns with the hydrophobic core of the membrane bilayer (Fig. 7D).

Intriguingly, we observed two layers of non-protein densities within the channel pore that align with the boundaries of the hydrophobic patch and the detergent micelle around the TMD in the cryo-EM maps for all classes (Fig. 7E). Similar densities have been observed in the structures of other large-pore channels, including pannexins and innexin (Burendei et al., 2020; Kuzuya et al., 2022). It is plausible that these densities are of a lipid bilayer that occupies the pore as illustrated in Fig. 7F. In this model, the hydrophobic acyl chains would occupy the space encircled by the hydrophobic patch, and the polar head groups would interact with the charged residues at the borders of the hydrophobic patch.

To confirm that these densities are not detergent-induced artifacts, we reconstituted the 8C-8A(IL1^{25}) chimera in lipid nanodiscs and performed cryo-EM analysis (Fig. 7–figure supplement 1). Although the resolution of the cryo-EM maps could not be improved beyond 7 Å, the same bilayer-like density within the channel pore was visible (Fig. 7–figure supplement 1). It is noteworthy that the lipid-like densities within the pores are similar in intensity and shape to the lipid densities observed around the protein within the nanodisc (Fig. 7–figure supplement 1).

DISCUSSION

Except for LRRC8A, homomeric LRRC8 channels do not traffic to the plasma membrane and cannot be functionally characterized (Voss et al., 2014; Yamada & Strange, 2018; Zhou et al., 2018). LRRC8A homomers form plasma membrane channels, but they exhibit abnormal functional properties. Most notably, LRRC8A channels are not activated by cell swelling under normal physiological conditions (Yamada et al., 2021b; Yamada & Strange, 2018) and are only weakly activated by extreme reductions in cytoplasmic ionic strength (Fig. 6–figure supplement 1) (Yamada et al., 2021b). LRRC8A channels also exhibit grossly abnormal DCPIB pharmacology (Yamada et al., 2021b). The non-native functional properties of LRRC8A

channels indicate that they have a non-native structure, which presents significant limitations for understanding how VRAC/LRRC8 channels are regulated and how pore structure determines solute permeability characteristics.

Homomeric LRRC8 channels with physiologically relevant functional properties are formed by chimeric proteins containing parts of the essential subunit LRRC8A and another LRRC8 paralog (Yamada & Strange, 2018). The 8C-8A(IL1^{25}) chimeric channel exhibits normal sensitivity to cell volume changes and intracellular ionic strength and normal DCPIB pharmacology (Fig. 6–figure supplement 1) (Yamada et al., 2021b; Yamada & Strange, 2018).

Unlike homomeric LRRC8A and LRRC8D channels, which are hexamers, our studies demonstrate that 8C-8A(IL1^{25}) chimeric channels have a heptameric structure (Figs. 2-3). The number of subunits required to form native VRAC/LRRC8 channels is unknown. However, native gel, crosslinking, and mass spectrometry studies (Syeda et al., 2016) and photobleaching experiments (Gaitán-Peñas et al., 2016) suggest that VRAC/LRRC8 channels are formed by ≥6 LRRC8 subunits.

The 8C-8A(IL1^{25}) has a limiting pore radius of 4.7 Å (Figs. 6 and Fig. 6–figure supplement 2A), which unlike the much narrower LRRC8A pore (Fig. 6 and Fig. 6–figure supplement 2B), is very consistent with the 6-7 Å pore radius estimated for native VRAC/LRRC8 channels (Droogmans et al., 1999; Ternovsky et al., 2004) and the role of these channels play in the transport of large anionic and uncharged organic solutes (Sabirov & Okada, 2005; Strange et al., 2019). A leucine residue located at position 105 forms the 8C-8A(IL1^{25}) pore constriction (Fig. 6A). In LRRC8A and LRRC8B, L105 is replaced by arginine. LRRC8D and LRRC8E paralogs have either phenylalanine or leucine at the homologous position. Hexameric LRRC8A and LRRC8D channels have limiting pore radii of 2.0 Å and 3.5 Å, respectively (Fig. 6B and Fig. 6–figure supplement 2). When we create hypothetical heptamers by aligning LRRC8A and LRRC8D subunits onto individual 8C-8A(IL1^{25}) subunits, the pore radii increase to 4.7 Å and 7.1 Å, respectively, indicating that the oligomeric state has a direct impact in pore size

and likely in channel transport properties (Fig. 6–figure supplement 2D-F). Consistent with this conclusion, LRRC8A hexameric channels have lower relative permeability to the large organic anions glutathione and lactobionate compared to heptameric 8C-8A(IL1^{25}) channels (Fig. 6D-E).

The narrow pore radius of 2 Å of the LRRC8A hexameric channel (Fig. 6B) also likely accounts for its abnormal DCPIB pharmacology. Native VRAC/LRRC8 channels are inhibited >90% by 10 μM DCPIB. Inhibition is voltage-insensitive and exhibits a Hill coefficient of 2.9 (Friard et al., 2017), suggesting that multiple DCPIB molecules are required to inhibit the channel. The DCPIB pharmacology of 8C-8A(IL1^{25}) recapitulates that of native VRAC/LRRC8 channels (Yamada et al., 2021b). In contrast, LRRC8A hexameric channels are weakly inhibited by 10 μM DCPIB, and inhibition is strongly voltage-dependent with a Hill coefficient close to 1 (Yamada et al., 2021b). The low Hill coefficient is consistent with a LRRC8A cryo-EM structure described by Kern et al. (Kern et al., 2019), showing a single DCPIB molecule blocking the channel pore at the narrowest constriction formed by R103 (Fig 6B).

Two recent studies have defined high-resolution cryo-EM structures of LRRC8A/LRRC8C heteromeric channels (Kern et al., 2022; Rutz et al., 2023). Both studies demonstrated that the heteromeric channels could adopt a hexameric conformation with a limiting pore radius of 2-3 Å, similar to that of LRRC8A hexamers. However, these channels either had 5:1 (Kern et al., 2022) or 4:2 LRRC8A:LRRC8C stoichiometries, indicating that LRRC8A:LRRC8C heteromers can adopt multiple oligomeric forms.

Taken together, existing cryo-EM structural data suggest that native VRAC/LRRC8 channels may exist in multiple oligomeric conformations, as has been reported for CALHM channels. It will be critical to relate the functional properties of various channel oligomeric conformations to those of native VRAC/LRRC8 channels. It will also be important to define the role of LRRC8A in channel assembly and conformation. Four groups have shown that LRRC8A has a dominant-negative function. Overexpression of LRRC8A suppresses endogenous (Qiu et

al., 2014; Syeda et al., 2016; Voss et al., 2014) and heterologously expressed (Yamada et al., 2016) VRAC/LRRC8 currents. LRRC8A protein levels may therefore impact channel assembly and function.

Kern et al. identified lipids located between individual subunits in LRRC8A hexameric channels reconstituted in lipid nanodiscs (Kern et al., 2019). Intersubunit non-protein densities, which are most likely lipids, are also observed between 8C-8A(IL1^{25}) subunits in detergent reconstituted channels (Fig. 7A). Importantly, we observed two layers of density resembling lipid bilayer blocking the pore of the 8C-8A(IL1^{25}) heptameric channel (Fig. 7B and Fig. 6–figure supplement 1). In agreement with our observations, in a recent pre-print reporting the hexameric structure of LRRC8A-LRRC8C (Kern et al. 2022), ordered lipid molecules are observed on the extracellular side of the pore opening aligning well with the densities we observed. Intrapore lipids have recently been proposed to be critical structural and regulatory elements of pannexins (Kuzuya et al., 2022) and closely related innexin (Burendei et al., 2020) and CALHM (Drożdżyk et al., 2020; Syrjanen et al., 2020) channels, as well as bacterial mechanosensitive channels (Rasmussen et al., 2019; Reddy et al., 2019; Zhang et al., 2021). Kuzuya et al. suggest that movement of lipids out of the pore through gaps between the subunits of the human pannexin 1 channel is required for channel opening (Kuzuya et al., 2022). A similar mechanism can be suggested for 8C-8A(IL1^{25}) heptameric channels. However, further experimental characterization is required to assess if lipids occupy the pore and play an essential role in channel gating.

Leucine-rich repeat motifs have been identified in over 14,000 proteins from viruses to eukaryotes and play essential roles in signal transduction and as sites for protein-protein interactions (Bella et al., 2008; Kobe & Kajava, 2001; Matsushima et al., 2019). The LRR motif can also function as a mechanosensor (Ju et al., 2016; Ju et al., 2015). VRAC/LRRC8 channels most likely arose by fusion of the transmembrane domain encoding portion of a pannexin channel gene with the LRR domain portion of an unrelated gene type (Abascal & Zardoya,

2012). Conformational changes in the VRAC/LRRC8 channel LRR domain are correlated with changes in channel activity (Deneka et al., 2021; König et al., 2019), and multiple cryo-EM structures demonstrate that this region is conformationally flexible (Fig. 5) (Deneka et al., 2021; Deneka et al., 2018; Kasuya et al., 2018; Kefauver et al., 2018; Kern et al., 2019; Nakamura et al., 2020). These data all point to the high likelihood that the VRAC/LRRC8 channel LRRD is a critical element of the channel's cell volume sensing apparatus.

LRRC8 chimeras with normal cell volume and ionic strength sensitivity must contain all or part of the LRRC8A IL1 (Yamada & Strange, 2018), indicating that this protein region is also critical for channel regulation. The 25 amino acid region of the LRRC8A IL1 inserted into the 8C-8A(IL1^{25}) chimera is predicted to be intrinsically disordered (Yamada & Strange, 2018). Consistent with this prediction, this region was not visible in our cryo-EM structures. It is conceivable that the LRRC8A IL1 is required for correct channel assembly and conformation, that it plays a direct role in cell volume sensing and/or that it functions to transduce cell volume-induced conformational changes into changes in the gating.

The mechanisms by which eukaryotic cells sense cell volume changes and transduce those changes into regulatory responses remain mysterious. Understanding how VRAC/LRRC8 channels detect cell volume is greatly constrained by the abnormal functional properties of LRRC8A homomers and by the undefined heteromeric nature of native channels. The high resolution cryo-EM structures of the 8C-8A(IL1^{25}) homomeric chimera, which has native physiological properties, has revealed several novel structural elements of VRAC/LRRC8 channels. These structures now provide the foundation for defining the molecular basis of channel cell volume sensing utilizing structure-guided mutagenesis combined with electrophysiological functional analysis of channels with defined stoichiometry and subunit arrangement.

METHODS

Constructs

Human LRRC8A and LRRC8C cDNAs cloned into pCMV6 were purchased from OriGene Technologies. The 8C-8A(IL1^{25}) chimera cDNA construct was generated using the Phusion High-Fidelity PCR kit (New England BioLabs). All cDNAs were tagged on their carboxy terminus with Myc-DDK epitopes. For protein expression, the cDNAs encoding human LRRC8A and the 8C-8A(IL1^{25}) chimera were sub-cloned with a C-terminal FLAG tag into pAceBac1 vectors and incorporated into baculovirus using the Multibac expression system (Fitzgerald et al., 2006). All constructs were verified by DNA sequencing.

Cell lines

Patch clamp experiments were performed using *Lrrc8*$^{-/-}$ HCT116 cell line in which the five *Lrrc8* genes were disrupted by genome editing. *Lrrc8*$^{-/-}$ cells were prepared and authenticated in the Thomas Jentsch Lab (Ullrich et al., 2016). They were a generous gift from Thomas Jentsch. The absence of VRAC/LRRC8 channel activity in the *Lrrc8*$^{-/-}$ cell line was confirmed routinely by patch clamp electrophysiology performed on cells transfected with GFP cDNA only.
The cells were tested negative for *Mycoplasma* contamination.

The cells were grown in McCoy's 5A media (HyClone) supplemented with 10 % fetal bovine serum (FBS) (R&D systems), 50 units/ml of penicillin, and 50µg/ml streptomycin in a humidified incubator at 37 °C with 5% CO_2.

Protein expression and purification

8C-8A(IL1^{25}) chimera was expressed in *Sf9* cells (4×10^6 cells/ml) at 27 °C for 48 hours. Cells were harvested by centrifugation (2,000x *g*) and resuspended in a lysis buffer composed of 150mM NaCl and 50 mM Tris-HCl, pH 8.0, 1 mM Phenylmethylulfonyl fluoride (PMSF). After cell lysis using Avastin EmulsiFlex-C3, the cell lysate was clarified from large debris by centrifugation at 6,000x *g* for 20 min. The cleared lysate was centrifuged at 185,000x *g* (Type

Ti45 rotor) for 1 h. Membrane pellets were resuspended and homogenized in ice-cold resuspension buffer (150 mM NaCl, 50 mM Tris-HCl, pH 8.0) and solubilized using 0.5% lauryl maltose neopentyl glycol (LMNG) at a membrane concentration of 100 mg/ml. The solubilized pellets were stirred gently for 4 h at 4 °C, and the insoluble material was separated by centrifugation at 185,000x *g* (Type Ti45 rotor) for 40 min. The supernatant was then mixed with anti-FLAG affinity gel resin (Sigma) at 4 °C for 1 hour. After washing the resin with 10 column volume wash buffer composed of 150 mM NaCl, 50 mM Tris-HCl, pH 8.0, and 0.005% LMNG, the protein was eluted using the wash buffer supplemented with 100μg/ml FLAG peptide. Protein was further purified by size exclusion chromatography using a Superose 6 Increase column (10/300 GL, GE Healthcare) equilibrated with 150 mM NaCl, 50 mM Tris-HCl, pH 8.0, 0.005% LMNG. The peak fraction corresponding to 8C-8A($IL1^{25}$) was concentrated to 3.0 mg/ml, centrifuged at 220,*000x g* using an S110-AT rotor (ThermoFisher Scientific) for 10 min, and used immediately for cryo-EM imaging. Human LRRC8A with a C-terminal Flag tag was purified using the same protocol described above for 8C-8A($IL1^{25}$).

For nanodisc incorporation, 8C-8A($IL1^{25}$) chimera was purified as described above except n-Dodecyl-β-D-Maltopyranoside (DDM, 1% for solubilization of the membrane and 0.05% in the purification buffers) was used instead of LMNG. The membrane scaffold protein MSP1E3D1 was expressed using the p MSP1E3D1 plasmid, a gift from Stephen Sligar (Addgene plasmid # 20066; http://n2t.net/addgene:20066; RRID: Addgene_20066) (Denisov et al., 2007). MSP1E3D1 was expressed in *E. coli* BL21(DE3) cells and purified as described previously using Ni^{2+} affinity resin (Ritchie et al., 2009). The histidine tag was cleaved off using TEV protease, and the protein was further purified by SEC using a HiLoad 16/600 Superdex 200 pg column equilibrated with 300 mM NaCl and 40 mM Tris-HCl, pH 8.0. Peak fractions containing MSP1E3D1 were collected and stored at -80°C for the nanodisc formation.

MSP1E3D1 Nanodisc formation

The preparation of nanodiscs was performed by mixing 8C-8A(IL1^{25}) purified in the presence of DDM with POPC lipids (Avanti Polar Lipids, Inc.) and MSP1E3D1 at a final molar ratio of 1:2.5:250 (8C-8A(IL1^{25}):MSP1E3D1:POPC). The mixture was incubated with Biobeads SM2 (Bio-Rad) overnight. After removing the biobeads by centrifugation, the protein sample was concentrated and purified by SEC using a Superose 6 10/300 Increase column equilibrated with 150 mM NaCl and 50 mM Tris-HCl, pH 8.0. Peak fractions corresponding to 8C-8A(IL1^{25})-MSP1E3D1 nanodiscs were concentrated to 2.0 mg/ml and used for cryoEM grid preparation immediately.

Cryo-EM sample preparation and data collection

Purified 8C-8A(IL1^{25}) was applied to 300 mesh UltrAuFoil holey gold 1.2/1.3 grids (Quantifoil Microtools) that were glow discharged for 10 seconds at 25 mA. The grids were blotted for 4 seconds at force 12 using double-layer Whatman filter papers (1442-005, GE Healthcare) before plunging into liquid ethane using an FEI MarkIV Vitrobot at 8 °C and 100% humidity. Samples were imaged using a 300 kV FEI Krios G3i microscope equipped with a Gatan K3 direct electron camera. Movies containing 40 frames were collected in super-resolution mode at 81,000x magnification with a physical pixel size of 1.1 Å/pixel and defocus values at a range of -0.8 to -1.5 µm using the automated imaging software SerialEM (Mastronarde, 2005).

8C-8A(IL1^{25}) nanodisc grids were prepared as described above. Samples were imaged using a 300 kV FEI Krios G4 microscope equipped with a Gatan K3 direct electron camera. Movies containing 50 frames were collected in super-resolution mode at 103,000x magnification with a physical pixel size of 0.818 Å/pixel and defocus values at a range of -0.8 to -2.2 µm using the automated imaging software EPU (ThermoFisher Scientific).

Cryo-EM data processing

All image processing was performed using CryoSparc2 (Punjani et al., 2017). Motion correction and CTF estimations were performed locally using Patch Motion Correction and Patch CTF Estimation procedures. Initial particle picking was performed by blob search. Particles were then binned 4x and extracted. After 2D classification, classes with clear structural features were selected and used for template-based particle picking. The new set of particles was binned four times and extracted. After 2D classification, a cleaned particle set was used for the ab initio 3D reconstruction. The resulting map was used as a model for 3D classification. After a series of 2D and 3D classification runs, particles were reextracted with a box size of 360x360 pixels. These particles were separated into six classes using 3D classification. Five out of six classes revealed interpretable density maps, and these particles were processed further using non-uniform refinement to obtain the final cryo-EM maps for each class.

To improve the quality of the cryo-EM maps around the ICDs, we performed local refinements using masks that cover the ICD of each subunit (Fig. 2–figure supplement 2). We observed a noticeable improvement in class 1 structure and used these maps for model building. We applied the same strategy for the LRRDs. However, the quality of the maps did not improve to a level allowing us to build reliable models.

Data processing for 8C-8A(IL1^{25}) nanodiscs was performed as described above, with the following exceptions. Motion correction was performed using MotionCor2 (Zheng et al., 2017) in Relion 3.0 (Zivanov et al., 2018). The final set of particles was extracted with a box size of 480x480 pixels, and they were classified into three 3D classes.

Model building

Models were built using Coot (Emsley & Cowtan, 2004). We initially placed the human LRRC8C model from the AlphaFold protein structure prediction database (Jumper et al., 2021; Varadi et al., 2022) in the class 1 density. We manually fitted the individual residues into the density while

removing the parts that did not have corresponding interpretable densities. Once we built a complete subunit, we copied the model into the other six protomers and manually fit individual residues into the density. The model was refined using Phenix real-space refinement (Afonine et al., 2018). We performed iterative build-refine cycles till a satisfactory model was obtained. The resulting model was fitted into the class 2 and 3 maps and fitted into the density using the same build-refine iterations as described above. Because of their limited resolution, most parts of class 5 and 6 structures were modeled without their side chains (i.e., as alanines) while maintaining their correct labeling for the amino acid type. The LRRDs were not modeled in all five structures. 8A-IL1^{25} is longer by 4 amino acids than the corresponding region in LRRC8C (Fig. 1). Therefore, the residue numbering after 8A(IL1^{25}) in the 8C-8A(IL1^{25}) chimera increases by 4 amino acids in the polypeptide. However, we kept the LRRC8C numberings in the models to facilitate easier comparison with other studies. Validations of the structural models were performed using MolProbity (Williams et al., 2018) implemented in Phenix (Afonine et al., 2018).

Some of the data processing and refinement software was supported by SBGrid (Morin et al., 2013).

Patch clamp electrophysiology

LRRC8A and 8C-8A(IL1^{25}) cDNA constructs were expressed in *Lrrc8*$^{-/-}$ HCT116 cells transfected using Turbofectin 8.0 (OriGene Technologies) with 0.125 µg GFP cDNA and 0.25 µg of 8A and 8C-8A(IL1^{25}).

Transfected cells were identified by GFP fluorescence and patch clamped in the whole cell mode at room temperature using patch electrodes pulled from 1.5 mm outer-diameter silanized borosilicate microhematocrit tubes. Recordings were not performed on cells where access resistance was >2-fold that of the pipette resistance.

The composition of the control bath and pipette solutions used in these studies is shown in Table 3. Intracellular ionic strength was reduced by the removal of CsCl or Cesium

methanesulfonate from the patch pipette solution and replacement with sucrose to maintain solution osmolality.

Whole-cell currents were measured with an Axopatch 200A (Axon Instruments) patch-clamp amplifier. Electrical connections to the patch-clamp amplifier were made using Ag/AgCl wires and 3M KCl/agar bridges. Series resistance was compensated by >85% to minimize voltage errors. Data acquisition and analysis were performed using pClamp 10 software (Axon Instruments).

Changes in current amplitude were quantified using a voltage-ramping protocol. Membrane voltage was held at -30mV throughout all experiments. Ramps were initiated by stepping membrane voltage to -100mV and then ramping membrane voltage over 1 s to +100mV. This was followed by a step back to -30mV for 4 s before the ramp was repeated.

Relative anion permeability (P_X/P_{Cl}) was measured from Cl^- substitute-induced changes in reversal potential using a modified Goldman–Hodgkin–Katz equation (Voss et al., 2014). LRRC8A and 8C-8A(IL1^{25}) currents were activated with low ionic strength, 0.062 M, patch pipette solution and by cell swelling induced by reducing bath osmolality to 250 mOsm. After stable current activation was achieved, changes in reversal potential were induced by replacing bath CsCl with either cesium glutathione or cesium lactobionate. Reversal potentials were corrected for anion-induced changes in liquid junction potentials.

Electrophysiological data are presented as means ± S.E.M. All patch clamps studies were performed on at least two independently transfected groups of cells. *n* represents the number of patch-clamped cells from which currents were recorded. Statistical significance was determined using Student's *t* test for unpaired means.

Figure preparation

Figures were prepared using Chimera (Pettersen et al., 2004), ChimeraX (Pettersen et al., 2021), and The PyMOL Molecular Graphics System (Version 2.0, Schrödinger, LLC). Calculation of the pore radii was performed using the software HOLE (Smart et al., 1996).

DATA AVAILABILITY

Cryo-EM maps and atomic coordinates are deposited to the Electron Microscopy Data Bank (EMDB) and Protein Data Bank (PDB) databases. The accession codes are EMD-27770 and 8DXN for class 1; EMD-27771 and 8DXO for class 2; EMD-27772 and 8DXP for class 3; EMD-27773 and 8DXQ for class 4; EMD-27774 and 8DXR for class 5.

ACKNOWLEDGEMENTS

We thank Dr. Kunpeng Lee at Case Western Reserve University and Melissa Chambers and Scott Collier at the Cryo-EM facility at Vanderbilt University for cryo-EM data collection. This work was conducted in part using the CPU and GPU resources of the Advanced Computing Center for Research and Education (ACCRE) at Vanderbilt University. We used the DORS storage system supported by the National Institute of Health (NIH) (S10 RR031634 to Jarrod Smith). This work was supported by the National Institute of Diabetes, Digestive, and Kidney Diseases Grant R01 DK51610 to JSD.

COMPETING INTERESTS

KS is cofounder and principal scientist of Revidia Therapeutics, Inc. None of the other authors have any conflicts of interest, financial or otherwise, to disclose.

FIGURE LEGENDS

Figure 1: Construct design of 8C-8A(IL1^{25}). A) Sequence alignment of LRRC8A and LRRC8C around the swapped IL1^{25} region. The swapped region in the 8C-8A(IL1^{25}) construct is shown inside a black box. The key below amino acid sequences denotes identical (*), conservative (:), and semi-conservative (.) sequences. Space indicates the residues that are not conserved. **B)** The amino acid sequence of the 8C-8A(IL1^{25}) construct around the swapped IL1^{25} region. **C)** Schematic diagram of the 8C-8A(IL1^{25}) protein highlighting the relative position of the swapped IL1^{25} region.

Figure 2: Cryo-EM structure of 8C-8A(IL1^{25}) A-B) Cryo-EM maps of 8C-8A(IL1^{25}) class 1 structure viewed through the membrane plane (**A**) and from the cytoplasm (**B**). **C**) Ribbon representation of the 8C-8A(IL1^{25}) class 1 structure viewed through the membrane plane. **D-E)** Unsharpened Cryo-EM maps of 8C-8A(IL1^{25}) class 1 structure viewed through the membrane plane (**D**) and from the cytoplasm (**E**), emphasizing low-resolution features. **F)** Structural comparison of the 8C-8A(IL1^{25}) (cyan) and LRRC8A (magenta, PDB ID: 5ZSU) subunits.

Figure 3: Subunit arrangement of the 8C-8A(IL1^{25}) chimera. A-B) Surface representation of the 8C-8A(IL1^{25}) class 1 structure viewed from two sides, highlighting the "tight" (**A**) and "loose" (**B**) interfaces. **C-E)** ICD, TMD, and ECDs are viewed from the cytoplasm with a depth of view, as shown in panel **B**.

Figure 4: Structural heterogeneity of 8C-8A(IL1^{25}) protomers. A) Structural comparison of the 8C-8A(IL1^{25}) subunits in the class 1 structure. The structures are aligned based on their ECDs. **B**) Close-up view of the box region in panel **A**, highlighting the structural differences in the loop that connects TM1 to EL1β1. Only two subunits are shown. **C)** Close-up view of the pore around the residues D50 and K51, which are shown as sticks. The residues that adopt different conformations compared to others are labeled in red. The dashed circle indicates the pore-lining surface. **D)** The same view as panel c but including the surface representation (transparent) to highlight the distinct interfaces between the subunits. **E-F)** Close-up view of the interfaces from the points of view shown in panel **D**.

Figure 5: Conformational heterogeneity of 8C-8A(IL1^{25}) chimeras. A-B) Cryo-EM maps (before sharpening) of 8C-8A(IL1^{25}) 3D classes viewed through the membrane plane (A) and from the cytoplasm (**B**). Individual subunits are colored as in Fig 1. The detergent micelle is shown in white. Red arrows point to the weak density of the LRRD, which is not located within the LRRD quaternary assembly. Lines represent the depth of the view for LRRD, ICD, and TMD. **C-D)** Ribbon representation of the ICD (**C**) and TMD (**D**) structures viewed from the cytoplasm with a depth of view indicated in panel A. The Cα atoms for G163 in ICD and V33 in TMD are shown as spheres. The distances between these atoms in neighboring subunits are shown as lines (in black and red for the tight and loose interfaces, respectively) and labeled in Å.

Figure 6: Comparison of channel pores. A-B) Pore openings of the 8C-8A(IL1^{25}) heptameric channel (class 1 structure) (**A**) and LRRC8A (PDB ID: 5ZSU) homohexameric channel (**B**) calculated using the software program HOLE (Smart et al., 1996). Only two opposing subunits are shown. Residues forming the constriction sites are shown as sticks. The first modeled residues at the N-termini are labeled as NT. **C**) 1D graph of the average radius along the length of the 8C-8A(IL1^{25}) (cyan) and LRRC8A (magenta) channel pores. **D**) Relative (P_x/P_{Cl}) glutathione and lactobionate permeabilities calculated from reversal potential changes induced

by replacing bath Cl^- with the test anion. Values are means ± SEM (N=4-7). **E**) Representative LRRC8A and 8C-8A(IL1^{25}) current traces in the presence of bath Cl^- or after substitution with glutathione ($Glut^-$) or lactobionate (Lac^-). Currents were elicited by ramping membrane voltage from −100 mV to +100 mV.

Figure 7: Interaction of lipids with the 8C-8A(IL1^{25}) chimera. A) Ribbon representation of the 8C-8A(IL1^{25}) class 1 structure along with the lipid-like cryo-EM densities (yellow) between the subunits viewed through the membrane plane. Loose and tight interfaces are indicated with arrows. **B**) Close-up views of the boxed regions in panel A. The cryo-EM map for the entire region visualized is shown as grey mesh. The phospholipid molecule shown as yellow sticks within the lipid-like density is used for illustration purposes only and not included in the deposited coordinate files. Select residues near the lipid-like densities are shown as sticks and labeled. **C-D)** Surface representation of the 8C-8A(IL1^{25}) pore colored based on electrostatic charge (**C**) and hydrophobicity (**D**). The hypothetical lipid bilayer around the TMD is built using CHARMM-GUI (Wu et al., 2014) and shown as sticks (cyan). Positioning of the protein within the bilayer is calculated using PPM 2.0 (Lomize et al., 2012). **E**) A sliced view of the unsharpened cryo-EM map (grey, transparent) with the ribbon representation of the 8C-8A(IL1^{25}) class 1 structure. Arrows indicate densities corresponding to pore-blocking lipid-like densities and detergent micelles. **F)** Hypothetical interaction of lipids with the inner surface of the pore is shown by placing phospholipids using CHARMM-GUI (Wu et al., 2014). Surface representation of the 8C-8A(IL1^{25}) colored based on hydrophobicity as in panel D.

FIGURE SUPPLEMENT LEGENDS

Figure 1 – figure supplement 1: Purification of 8C-8A(IL1^{25}). SDS-PAGE (**A**) and native PAGE (**B**) and size exclusion chromatography (**C**) analysis of the purified LRRC8A and 8C-8A(IL1^{25}) proteins.

Figure 2 – figure supplement 1: Cryo-EM analysis of 8C-8A(IL1^{25}). Flowchart detailing the particle selection and refinement procedure to obtain the cryo-EM maps of 8C-8A(IL1^{25}). Local resolution maps are shown on maps viewed at two different thresholds in Chimera. FSC curves and angular distributions are shown for the refined classes.

Figure 2 – figure supplement 2: Cryo-EM analysis of 8C-8A(IL1^{25}). A) Cryo-EM map of 8C-8A(IL1^{25}) class 1 structure colored by individual subunits. **B**) Masks used for local refinement of individual subunits are shown as transparent grey surfaces. Each mask was used separately for local refinement. **C**) The cryo-EM maps after local refinement for each subunit are aligned onto the original map. **D**) Ribbon representation of the 8C-8A(IL1^{25}) structure. **E-F**) Representative images of the cryo-EM density and the modeled structure covering parts of ECD (**E**), TMD (**F**), and ICD (**G**). The map in panel **G** is obtained after local refinement, and the maps in panels **E** and **F** are the original maps.

Figure 2 – figure supplement 3: Structural comparison of 8C-8A(IL1^{25}) to LRRC8A and pannexins. A-C) Ribbon representations of LRRC8A (PBD ID: 5ZSU) (**A**), 8C-8A(IL1^{25}) class 1

structure (**B**), and Pannexin 1 (PDB ID: 6VD7) (**C**) viewed from the extracellular space (top), through the membrane plane (middle) and from the cytoplasm (bottom). LRRDs for 8C-8A(IL1^{25}) and LRRC8A were not shown. Each subunit is colored differently.

Figure 3 – figure supplement 1: Comparison of subunit interfaces. A) Overlay of two 8C-8A(IL1^{25}) subunit pairs of the class 1 structure that form tight and loose interfaces. Structures were aligned on their ECDs. **B-C**) Close-up view of the ECDs forming the tight (**B**) and loose (**C**) interfaces. Select residues at the interfaces are shown in stick representation and labeled.

Figure 3 – figure supplement 2: Comparison of subunit interfaces. A) Overlay of two 8C-8A(IL1^{25}) subunit pairs of the class 1 structure that form tight and loose interfaces. Structures were aligned on their ECDs. **B-C**) Close-up view of the TMDs forming the tight (**B**) and loose (**C**) interfaces. Select residues at the interfaces are shown in stick representation and labeled.

Figure 3 – figure supplement 3: Comparison of subunit interfaces. A) Overlay of two 8C-8A(IL1^{25}) subunit pairs of the class 1 structure that form tight and loose interfaces. Structures were aligned on their ECDs. **B-C**) Close-up view of the ICDs forming the tight (**B**) and loose (**C**) interfaces. Select residues at the interfaces are shown in stick representation and labeled.

Figure 5 – figure supplement 1: Comparison of 8C-8A(IL1^{25}) structures. A) Overlay of 8C-8A(IL1^{25}) structures in different classes viewed through the membrane plane. **B-D**) Overlay of 8C-8A(IL1^{25}) structures in different classes viewed from the intracellular space focusing on the ECD (**B**), TMD (**C**), and ICD (**D**). Structures are aligned on their ECDs and colored as indicated in the figure. The depths of the views for panels **B-D** are indicated in panel **A** with straight lines.

Figure 5 – figure supplement 2: Comparison of the D40-K51 loop among different classes. Close-up view of the pore around the residues D50 and K51, which are shown as sticks. The residues that adopt different conformations compared to others are labeled in red. The dashed circle indicates the pore-lining surface.

Figure 6 – figure supplement 1: Effect of intracellular ionic strength on activation of LRRC8A and the 8C-8A(IL1^{25}) chimeric channel. The relative current was quantified as the fold change in current measured immediately after whole-cell access was achieved and currents measured 120 sec later. As we have shown previously (Yamada et al., 2021a), LRRC8A currents activate only very slowly when intracellular ionic strength is reduced from a normal level of 0.162 M to 0.062 M. However, no statistically significant (P>0.9) current activation is detected 120 sec after whole-cell access even at the lowest intracellular ionic strength of 0.062 M. In striking contrast, significant (P=0.02) 8C-8A(IL1^{25}) current is detected at an intracellular ionic strength of 0.136 M. Reducing ionic strength further leads to more rapid current activation and larger current amplitudes measured at 120 sec. The effect of ionic strength on the rate of 8C-8A(IL1^{25}) current activation is similar to what we have reported previously for native VRAC/LRRC8 channels(Cannon et al., 1998). The current amplitude was quantified at +60 mV above the measured reversal potential. Values are means ± SEM (N=5-8).

Figure 6 – figure supplement 2: Heptameric oligomerization leads to larger pore sizes. A-C) Close-up cytoplasmic view of the narrowest constriction sites of 8C-8A(IL1^{25}) class 1 structure (**A**), LRRC8A (PDB ID: 5ZSU) (**B**), and LRRC8D (PDB ID: 6M04) (**C**). **D**) The heptameric LRRC8A and LRRC8D models were obtained by overlaying one of the LRRC8A or LRRC8D subunits on the seven subunits of 8C-8A(IL1^{25}) heptamer by aligning the ECDs. **E-F**) Pores of hypothetical LRRC8A (**E**) and LRRC8D (**F**) heptamers. Residues forming the constriction are shown as sticks. The circles and the dashed lines represent the solvent-

accessible pore size and radius, respectively. The radii of the pores were calculated using the software HOLE (Smart et al., 1996) and shown on top of each panel.

Figure 7 – figure supplement 1: Cryo-EM analysis of 8C-8A(IL1^{25}) reconstituted in nanodiscs. A) Flowchart detailing the particle selection and refinement procedure to obtain the cryo-EM maps of the 8C-8A(IL1^{25}) nanodiscs. FSC curves and angular distributions are shown. **B-C**) Full (**B**) and sliced (**C**) views of the cryo-EM maps of the 8C-8A(IL1^{25}) nanodiscs.

Figure 1 – supplement 1 – source data 1: Raw and annotated images of the SDS-PAGE gel analyzing the purified LRRC8A and 8C-8A(IL1^{25}) proteins.

Figure 1 – supplement 1 – source data 2: Raw and annotated images of the native-PAGE gel analyzing the purified LRRC8A and 8C-8A(IL1^{25}) proteins.

684 **Table 1: Cryo-EM data collection, refinement, and validation statistics**

Data collection and processing					
Microscope	FEI Krios G3i microscope				
Detector	Gatan K3 direct electron camera				
Nominal magnification	81,000 x				
Voltage (kV)	300				
Electron exposure (e/Å^2)	54				
Defocus range (μm)	-0.8 to -1.5				
Pixel size (Å)	1.1				
Number of Micrographs	3,198				
Particles images (no.)	846,122				
Conformational state	**Class 1**	**Class 2**	**Class 3**	**Class 4**	**Class 5**
Symmetry imposed	C1	C1	C1	C1	C1
Final particles images (no.)	203,011	132,722	100,772	93,179	85,591
Map resolution (Å) (FSC threshold=0.143)	3.4	3.6	3.7	3.8	4.0
Refinement					
Model resolution (Å) (original map, FSC threshold=0.5)	3.6	3.9	3.9	4.2	4.4
B-factor used for map sharpening (Å^2)	-102.0	-88.2	-84.7	-70.5	-83
Model composition					
Non-hydrogen atoms	17,499	17,499	17,465	10,435	10,435
Protein residues	2,101	2,101	2,097	2,101	2,101
Mean B factors (Å^2)					
Protein	32.4	23.5	32.4	44.9	38.34
R.m.s. deviations					
Bond lengths (Å)	0.003	0.002	0.003	0.002	0.004
Bond angles (°)	0.563	0.525	0.553	0.516	0.807
Molprobity score	1.72	1.68	1.75	1.37	1.49
Clash score	5.04	4.84	6.02	1.14	1.54
Poor rotamers (%)	0.0	0.0	0.0	0.0	0.0
Favored (%)	92.9	93.5	93.6	89.95	88.3
Allowed (%)	7.1	6.5	6.4	10.0	11.6
Disallowed (%)	0	0	0	0.05	0.1

685

Table 2: Analysis of the total buried solvent accessible surface area between subunits for each domain in the class 1 structure.

	Buried surface area between the neighboring subunits (Å^2)[1]						
	Subunits A-B	Subunits B-C	Subunits C-D	**Subunits D-E**	Subunits E-F	Subunits F-G	**Subunits G-A**
	tight	tight	tight	**loose**	tight	tight	**loose**
ECD[2]	1,995	1,897	1,964	**1905**	1,900	1,896	**1,869**
TMD[2]	664	625	620	**122**	660	670	**99**
ICD[2]	462	294	500	**0**	559	502	**0**

[1] Buried solvent accessible surface area calculations were performed using the software NACCESS v2.1.1 (Hubbard & Thornton, 1993).

[2] Domain definitions used for these calculations are as follows: ECD: Residues 49-121 and 288-310; TMD: residues 20-48, 122-150, 260-287, and 311-342; ICD: residues 151-259 and 343-405.

Table 3. Composition of patch pipette and solutions.

	Patch pipette solutions			**Bath solutions**	
	Control	**Control**		**Control**	**Hypotonic**
CsCl	126 mM	26 mM		75 mM	75 mM
Cs methanesulfonate		100 mM			
$MgSO_4$	2 mM	2 mM		5 mM	5 mM
Ca-gluconate$_2$				1 mM	1 mM
ATP-Na_2	2 mM	2 mM			
GTP-Na_2	0.5 mM	0.5 mM			
Glutamine				2 mM	2 mM
EGTA	1 mM	1 mM			
HEPES	20 mM	20 mM		12 mM	12 mM
Tris				8 mM	8 mM
CsOH	12 mM	12 mM			
HCl				2 mM	2 mM
Glucose				5 mM	5 mM
Sucrose	16 mM	16 mM		115 mM	70 mM
pH[1]	7.2	7.2		7.4	7.4
Osmolality	275 mOsm	275 mOsm		300 mOsm	250 mOsm
Ionic strength	0.162 M	0.162 M			

[1] The pH of patch pipette and bath solutions was adjusted with CsOH and HCl, respectively.

REFERENCES

Abascal, F., & Zardoya, R. (2012). LRRC8 proteins share a common ancestor with pannexins, and may form hexameric channels involved in cell-cell communication. *Bioessays, 34*(7), 551-560. doi:10.1002/bies.201100173

Afonine, P. V., Poon, B. K., Read, R. J., Sobolev, O. V., Terwilliger, T. C., Urzhumtsev, A., & Adams, P. D. (2018). Real-space refinement in PHENIX for cryo-EM and crystallography. *Acta Crystallogr D Struct Biol, 74*(Pt 6), 531-544. doi:10.1107/s2059798318006551

Bella, J., Hindle, K. L., McEwan, P. A., & Lovell, S. C. (2008). The leucine-rich repeat structure. *Cell Mol Life Sci, 65*(15), 2307-2333. doi:10.1007/s00018-008-8019-0

Bhat, E. A., & Sajjad, N. (2021). Human Pannexin 1 channel: Insight in structure-function mechanism and its potential physiological roles. *Mol Cell Biochem, 476*(3), 1529-1540. doi:10.1007/s11010-020-04002-3

Burendei, B., Shinozaki, R., Watanabe, M., Terada, T., Tani, K., Fujiyoshi, Y., & Oshima, A. (2020). Cryo-EM structures of undocked innexin-6 hemichannels in phospholipids. *Sci Adv, 6*(7), eaax3157. doi:10.1126/sciadv.aax3157

Cannon, C. L., Basavappa, S., & Strange, K. (1998). Intracellular ionic strength regulates the volume sensitivity of a swelling-activated anion channel. *Am J Physiol, 275*(2), C416-422. doi:10.1152/ajpcell.1998.275.2.C416

Deneka, D., Rutz, S., Hutter, C. A. J., Seeger, M. A., Sawicka, M., & Dutzler, R. (2021). Allosteric modulation of LRRC8 channels by targeting their cytoplasmic domains. *Nat Commun, 12*(1), 5435. doi:10.1038/s41467-021-25742-w

Deneka, D., Sawicka, M., Lam, A. K. M., Paulino, C., & Dutzler, R. (2018). Structure of a volume-regulated anion channel of the LRRC8 family. *Nature, 558*(7709), 254-259. doi:10.1038/s41586-018-0134-y

Deng, Z., He, Z., Maksaev, G., Bitter, R. M., Rau, M., Fitzpatrick, J. A. J., & Yuan, P. (2020). Cryo-EM structures of the ATP release channel pannexin 1. *Nat Struct Mol Biol, 27*(4), 373-381. doi:10.1038/s41594-020-0401-0

Denisov, I. G., Baas, B. J., Grinkova, Y. V., & Sligar, S. G. (2007). Cooperativity in cytochrome P450 3A4: linkages in substrate binding, spin state, uncoupling, and product formation. *J Biol Chem, 282*(10), 7066-7076. doi:10.1074/jbc.M609589200

Droogmans, G., Maertens, C., Prenen, J., & Nilius, B. (1999). Sulphonic acid derivatives as probes of pore properties of volume-regulated anion channels in endothelial cells. *Br J Pharmacol, 128*(1), 35-40. doi:10.1038/sj.bjp.0702770

Drożdżyk, K., Sawicka, M., Bahamonde-Santos, M. I., Jonas, Z., Deneka, D., Albrecht, C., & Dutzler, R. (2020). Cryo-EM structures and functional properties of CALHM channels of the human placenta. *Elife, 9*. doi:10.7554/eLife.55853

Emsley, P., & Cowtan, K. (2004). Coot: model-building tools for molecular graphics. *Acta Crystallogr D Biol Crystallogr, 60*(Pt 12 Pt 1), 2126-2132. doi:10.1107/s0907444904019158

Fitzgerald, D. J., Berger, P., Schaffitzel, C., Yamada, K., Richmond, T. J., & Berger, I. (2006). Protein complex expression by using multigene baculoviral vectors. *Nat Methods, 3*(12), 1021-1032. doi:10.1038/nmeth983

Friard, J., Tauc, M., Cougnon, M., Compan, V., Duranton, C., & Rubera, I. (2017). Comparative Effects of Chloride Channel Inhibitors on LRRC8/VRAC-Mediated Chloride Conductance. *Front Pharmacol, 8*, 328. doi:10.3389/fphar.2017.00328

Gaitán-Peñas, H., Gradogna, A., Laparra-Cuervo, L., Solsona, C., Fernández-Dueñas, V., Barrallo-Gimeno, A., . . . Estévez, R. (2016). Investigation of LRRC8-Mediated Volume-Regulated Anion Currents in Xenopus Oocytes. *Biophys J, 111*(7), 1429-1443. doi:10.1016/j.bpj.2016.08.030

Hubbard, S., & Thornton, J. (1993). *NACCESS, Computer Program*. Department of Biochemistry Molecular Biology, University College London.
Jentsch, T. J. (2016a). VRACs and other ion channels and transporters in the regulation of cell volume and beyond. *Nat. Rev. Mol. Cell Biol, 17*(5), 293-307.
Jentsch, T. J. (2016b). VRACs and other ion channels and transporters in the regulation of cell volume and beyond. *Nat Rev Mol Cell Biol, 17*(5), 293-307. doi:10.1038/nrm.2016.29
Jin, Q., Zhang, B., Zheng, X., Li, N., Xu, L., Xie, Y., . . . Ye, S. (2020). Cryo-EM structures of human pannexin 1 channel. *Cell Res, 30*(5), 449-451. doi:10.1038/s41422-020-0310-0
Ju, L., Chen, Y., Xue, L., Du, X., & Zhu, C. (2016). Cooperative unfolding of distinctive mechanoreceptor domains transduces force into signals. *Elife, 5*. doi:10.7554/eLife.15447
Ju, L., Lou, J., Chen, Y., Li, Z., & Zhu, C. (2015). Force-Induced Unfolding of Leucine-Rich Repeats of Glycoprotein Ibα Strengthens Ligand Interaction. *Biophys J, 109*(9), 1781-1784. doi:10.1016/j.bpj.2015.08.050
Jumper, J., Evans, R., Pritzel, A., Green, T., Figurnov, M., Ronneberger, O., . . . Hassabis, D. (2021). Highly accurate protein structure prediction with AlphaFold. *Nature, 596*(7873), 583-589. doi:10.1038/s41586-021-03819-2
Kasuya, G., Nakane, T., Yokoyama, T., Jia, Y., Inoue, M., Watanabe, K., . . . Nureki, O. (2018). Cryo-EM structures of the human volume-regulated anion channel LRRC8. *Nat Struct Mol Biol, 25*(9), 797-804. doi:10.1038/s41594-018-0109-6
Kefauver, J. M., Saotome, K., Dubin, A. E., Pallesen, J., Cottrell, C. A., Cahalan, S. M., . . . Patapoutian, A. (2018). Structure of the human volume regulated anion channel. *Elife, 7*. doi:10.7554/eLife.38461
Kern, D. M., Bleier, J., Mukherjee, S., Hill, J. M., Kossiakoff, A. A., Isacoff, E. Y., & Brohawn, S. G. (2022). Structural basis for assembly and lipid-mediated gating of LRRC8A:C volume-regulated anion channels. *bioRxiv*, 2022.2007.2031.502239. doi:10.1101/2022.07.31.502239
Kern, D. M., Oh, S., Hite, R. K., & Brohawn, S. G. (2019). Cryo-EM structures of the DCPIB-inhibited volume-regulated anion channel LRRC8A in lipid nanodiscs. *Elife, 8*. doi:10.7554/eLife.42636
Kobe, B., & Kajava, A. V. (2001). The leucine-rich repeat as a protein recognition motif. *Curr Opin Struct Biol, 11*(6), 725-732. doi:10.1016/s0959-440x(01)00266-4
König, B., Hao, Y., Schwartz, S., Plested, A. J., & Stauber, T. (2019). A FRET sensor of C-terminal movement reveals VRAC activation by plasma membrane DAG signaling rather than ionic strength. *Elife, 8*. doi:10.7554/eLife.45421
Kuzuya, M., Hirano, H., Hayashida, K., Watanabe, M., Kobayashi, K., Terada, T., . . . Oshima, A. (2022). Structures of human pannexin-1 in nanodiscs reveal gating mediated by dynamic movement of the N terminus and phospholipids. *Sci Signal, 15*(720), eabg6941. doi:10.1126/scisignal.abg6941
Lomize, M. A., Pogozheva, I. D., Joo, H., Mosberg, H. I., & Lomize, A. L. (2012). OPM database and PPM web server: resources for positioning of proteins in membranes. *Nucleic Acids Res, 40*(Database issue), D370-376. doi:10.1093/nar/gkr703
Mastronarde, D. N. (2005). Automated electron microscope tomography using robust prediction of specimen movements. *J Struct Biol, 152*(1), 36-51. doi:10.1016/j.jsb.2005.07.007
Matsushima, N., Takatsuka, S., Miyashita, H., & Kretsinger, R. H. (2019). Leucine Rich Repeat Proteins: Sequences, Mutations, Structures and Diseases. *Protein Pept Lett, 26*(2), 108-131. doi:10.2174/0929866526666181208170027
Michalski, K., Syrjanen, J. L., Henze, E., Kumpf, J., Furukawa, H., & Kawate, T. (2020). The Cryo-EM structure of pannexin 1 reveals unique motifs for ion selection and inhibition. *Elife, 9*. doi:10.7554/eLife.54670
Morin, A., Eisenbraun, B., Key, J., Sanschagrin, P. C., Timony, M. A., Ottaviano, M., & Sliz, P. (2013). Collaboration gets the most out of software. *Elife, 2*, e01456. doi:10.7554/eLife.01456

Mou, L., Ke, M., Song, M., Shan, Y., Xiao, Q., Liu, Q., . . . Deng, D. (2020). Structural basis for gating mechanism of Pannexin 1 channel. *Cell Res, 30*(5), 452-454. doi:10.1038/s41422-020-0313-x

Nakamura, R., Numata, T., Kasuya, G., Yokoyama, T., Nishizawa, T., Kusakizako, T., . . . Nureki, O. (2020). Cryo-EM structure of the volume-regulated anion channel LRRC8D isoform identifies features important for substrate permeation. *Commun Biol, 3*(1), 240. doi:10.1038/s42003-020-0951-z

Pettersen, E. F., Goddard, T. D., Huang, C. C., Couch, G. S., Greenblatt, D. M., Meng, E. C., & Ferrin, T. E. (2004). UCSF Chimera--a visualization system for exploratory research and analysis. *J Comput Chem, 25*(13), 1605-1612. doi:10.1002/jcc.20084

Pettersen, E. F., Goddard, T. D., Huang, C. C., Meng, E. C., Couch, G. S., Croll, T. I., . . . Ferrin, T. E. (2021). UCSF ChimeraX: Structure visualization for researchers, educators, and developers. *Protein Sci, 30*(1), 70-82. doi:10.1002/pro.3943

Punjani, A., Rubinstein, J. L., Fleet, D. J., & Brubaker, M. A. (2017). cryoSPARC: algorithms for rapid unsupervised cryo-EM structure determination. *Nat Methods, 14*(3), 290-296. doi:10.1038/nmeth.4169

Qiu, Z., Dubin, A. E., Mathur, J., Tu, B., Reddy, K., Miraglia, L. J., . . . Patapoutian, A. (2014). SWELL1, a plasma membrane protein, is an essential component of volume-regulated anion channel. *Cell, 157*(2), 447-458. doi:10.1016/j.cell.2014.03.024

Qu, R., Dong, L., Zhang, J., Yu, X., Wang, L., & Zhu, S. (2020). Cryo-EM structure of human heptameric Pannexin 1 channel. *Cell Res, 30*(5), 446-448. doi:10.1038/s41422-020-0298-5

Rasmussen, T., Flegler, V. J., Rasmussen, A., & Böttcher, B. (2019). Structure of the Mechanosensitive Channel MscS Embedded in the Membrane Bilayer. *J Mol Biol, 431*(17), 3081-3090. doi:10.1016/j.jmb.2019.07.006

Reddy, B., Bavi, N., Lu, A., Park, Y., & Perozo, E. (2019). Molecular basis of force-from-lipids gating in the mechanosensitive channel MscS. *Elife, 8*. doi:10.7554/eLife.50486

Ritchie, T. K., Grinkova, Y. V., Bayburt, T. H., Denisov, I. G., Zolnerciks, J. K., Atkins, W. M., & Sligar, S. G. (2009). Chapter 11 - Reconstitution of membrane proteins in phospholipid bilayer nanodiscs. *Methods Enzymol, 464*, 211-231. doi:10.1016/s0076-6879(09)64011-8

Ruan, Z., Orozco, I. J., Du, J., & Lü, W. (2020). Structures of human pannexin 1 reveal ion pathways and mechanism of gating. *Nature, 584*(7822), 646-651. doi:10.1038/s41586-020-2357-y

Rutz, S., Deneka, D., Dittmann, A., Sawicka, M., & Dutzler, R. (2022). Structure of a volume-regulated heteromeric LRRC8A/C channel. *bioRxiv*, 2022.2008.2003.502623. doi:10.1101/2022.08.03.502623

Rutz, S., Deneka, D., Dittmann, A., Sawicka, M., & Dutzler, R. (2023). Structure of a volume-regulated heteromeric LRRC8A/C channel. *Nat Struct Mol Biol, 30*(1), 52-61. doi:10.1038/s41594-022-00899-0

Sabirov, R. Z., & Okada, Y. (2005). ATP release via anion channels. *Purinergic Signal, 1*(4), 311-328. doi:10.1007/s11302-005-1557-0

Smart, O. S., Neduvelil, J. G., Wang, X., Wallace, B. A., & Sansom, M. S. (1996). HOLE: a program for the analysis of the pore dimensions of ion channel structural models. *J Mol Graph, 14*(6), 354-360, 376. doi:10.1016/s0263-7855(97)00009-x

Strange, K., Yamada, T., & Denton, J. S. (2019). A 30-year journey from volume-regulated anion currents to molecular structure of the LRRC8 channel. *J Gen Physiol, 151*(2), 100-117. doi:10.1085/jgp.201812138

Syeda, R., Qiu, Z., Dubin, A. E., Murthy, S. E., Florendo, M. N., Mason, D. E., . . . Patapoutian, A. (2016). LRRC8 Proteins Form Volume-Regulated Anion Channels that Sense Ionic Strength. *Cell, 164*(3), 499-511. doi:10.1016/j.cell.2015.12.031

Syrjanen, J. L., Michalski, K., Chou, T. H., Grant, T., Rao, S., Simorowski, N., . . . Furukawa, H. (2020). Structure and assembly of calcium homeostasis modulator proteins. *Nat Struct Mol Biol, 27*(2), 150-159. doi:10.1038/s41594-019-0369-9

Ternovsky, V. I., Okada, Y., & Sabirov, R. Z. (2004). Sizing the pore of the volume-sensitive anion channel by differential polymer partitioning. *FEBS Lett, 576*(3), 433-436. doi:10.1016/j.febslet.2004.09.051

Ullrich, F., Reincke, S. M., Voss, F. K., Stauber, T., & Jentsch, T. J. (2016). Inactivation and Anion Selectivity of Volume-regulated Anion Channels (VRACs) Depend on C-terminal Residues of the First Extracellular Loop. *J Biol Chem, 291*(33), 17040-17048. doi:10.1074/jbc.M116.739342

Varadi, M., Anyango, S., Deshpande, M., Nair, S., Natassia, C., Yordanova, G., . . . Velankar, S. (2022). AlphaFold Protein Structure Database: massively expanding the structural coverage of protein-sequence space with high-accuracy models. *Nucleic Acids Res, 50*(D1), D439-d444. doi:10.1093/nar/gkab1061

Voss, F. K., Ullrich, F., Münch, J., Lazarow, K., Lutter, D., Mah, N., . . . Jentsch, T. J. (2014). Identification of LRRC8 heteromers as an essential component of the volume-regulated anion channel VRAC. *Science, 344*(6184), 634-638. doi:10.1126/science.1252826

Williams, C. J., Headd, J. J., Moriarty, N. W., Prisant, M. G., Videau, L. L., Deis, L. N., . . . Richardson, D. C. (2018). MolProbity: More and better reference data for improved all-atom structure validation. *Protein Sci, 27*(1), 293-315. doi:10.1002/pro.3330

Wu, E. L., Cheng, X., Jo, S., Rui, H., Song, K. C., Dávila-Contreras, E. M., . . . Im, W. (2014). CHARMM-GUI Membrane Builder toward realistic biological membrane simulations. *J Comput Chem, 35*(27), 1997-2004. doi:10.1002/jcc.23702

Yamada, T., Denton, J. S., & Strange, K. (2021a). LRRC8A homohexameric channels poorly recapitulate VRAC regulation and pharmacology. *Am. J Physiol Cell Physiol, 320* (3), C293-C303. doi:doi: 10.1152/ajpcell.00454.2020

Yamada, T., Figueroa, E. E., Denton, J. S., & Strange, K. (2021b). LRRC8A homohexameric channels poorly recapitulate VRAC regulation and pharmacology. *Am J Physiol Cell Physiol, 320*(3), C293-c303. doi:10.1152/ajpcell.00454.2020

Yamada, T., & Strange, K. (2018). Intracellular and extracellular loops of LRRC8 are essential for volume-regulated anion channel function. *J Gen Physiol, 150*(7), 1003-1015. doi:10.1085/jgp.201812016

Yamada, T., Wondergem, R., Morrison, R., Yin, V. P., & Strange, K. (2016). Leucine-rich repeat containing protein LRRC8A is essential for swelling-activated Cl- currents and embryonic development in zebrafish. *Physiol Rep, 4*(19). doi:10.14814/phy2.12940

Zhang, Y., Daday, C., Gu, R. X., Cox, C. D., Martinac, B., de Groot, B. L., & Walz, T. (2021). Visualization of the mechanosensitive ion channel MscS under membrane tension. *Nature, 590*(7846), 509-514. doi:10.1038/s41586-021-03196-w

Zheng, S. Q., Palovcak, E., Armache, J. P., Verba, K. A., Cheng, Y., & Agard, D. A. (2017). MotionCor2: anisotropic correction of beam-induced motion for improved cryo-electron microscopy. *Nat Methods, 14*(4), 331-332. doi:10.1038/nmeth.4193

Zhou, P., Polovitskaya, M. M., & Jentsch, T. J. (2018). LRRC8 N termini influence pore properties and gating of volume-regulated anion channels (VRACs). *J Biol Chem, 293*(35), 13440-13451. doi:10.1074/jbc.RA118.002853

Zivanov, J., Nakane, T., Forsberg, B. O., Kimanius, D., Hagen, W. J., Lindahl, E., & Scheres, S. H. (2018). New tools for automated high-resolution cryo-EM structure determination in RELION-3. *Elife, 7*. doi:10.7554/eLife.42166

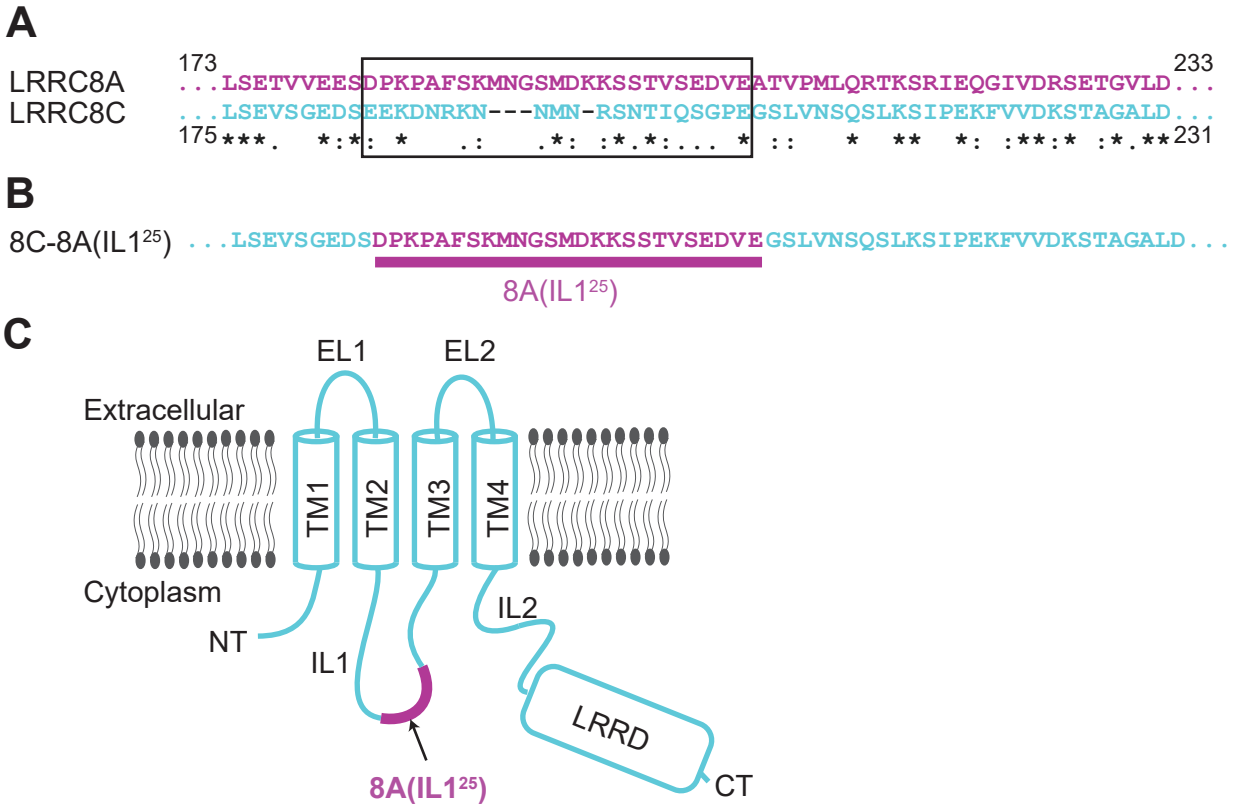
A
173
LRRC8A ...LSETVVEESDPKPAFSKMNGSMDKKSSTVSEDVEATVPMLQRTKSRIEQGIVDRSETGVLD...
LRRC8C ...LSEVSGEDSEEKDNRKN---NMN-RSNTIQSGPEGSLVNSQSLKSIPEKFVVDKSTAGALD...
175 231
B
8C-8A(IL1[25]) ...LSEVSGEDSDPKPAFSKMNGSMDKKSSTVSEDVEGSLVNSQSLKSIPEKFVVDKSTAGALD...
8A(IL1[25])
C
EL1
EL2
Extracellular
TM1
TM2
TM3
TM4
Cytoplasm
NT
IL1
IL2
LRRD
CT
8A(IL1[25])

Figure 1

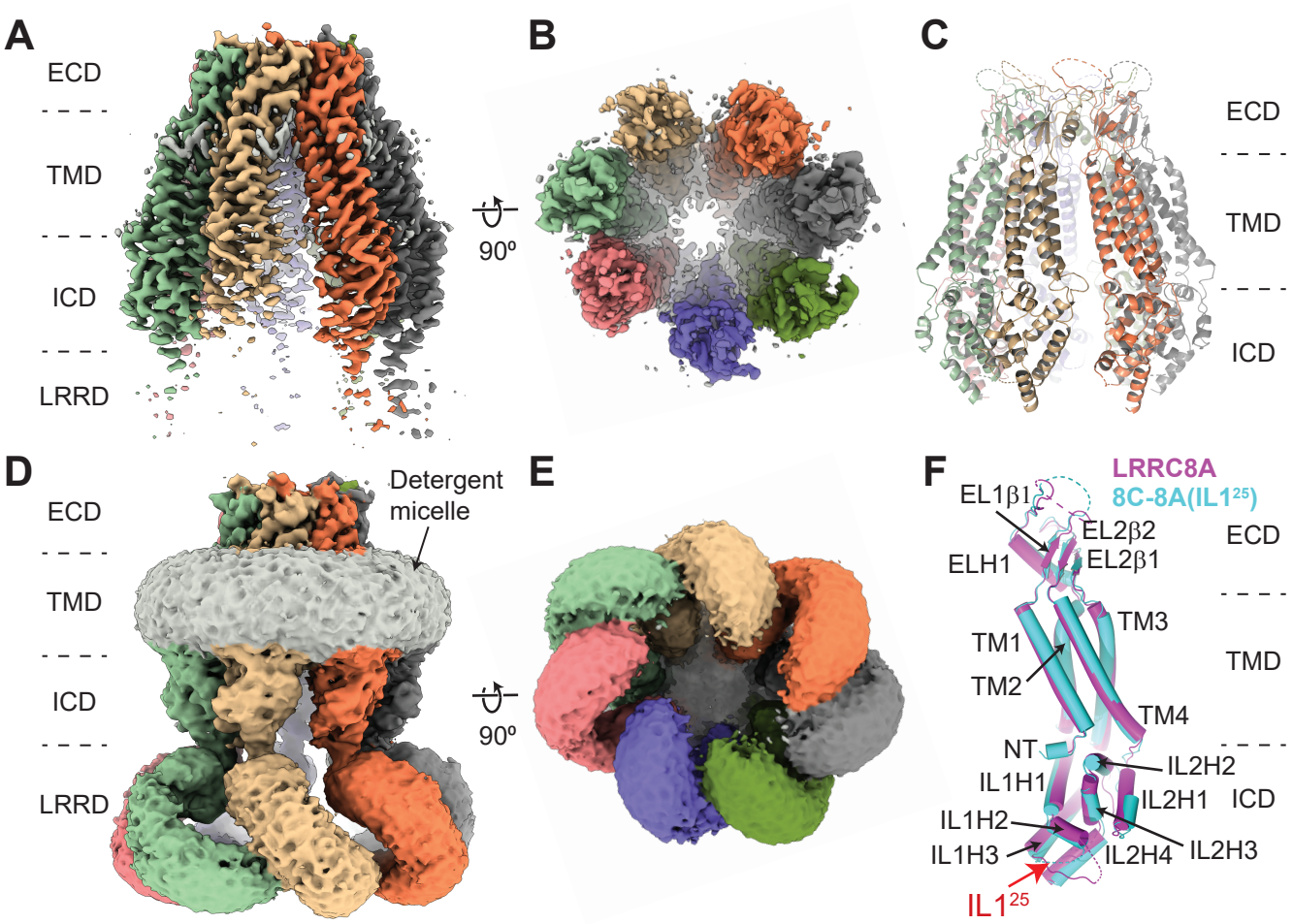
A
ECD
TMD
ICD
LRRD
90º
B
C
ECD
TMD
ICD
D
Detergent micelle
ECD
TMD
ICD
LRRD
90º
E
F
LRRC8A
8C-8A(IL1²⁵)
EL1β1
EL2β2
EL2β1
ELH1
TM3
TM1
TM2
TM4
NT
IL2H2
IL1H1
IL2H1
IL1H2
IL1H3
IL2H4
IL2H3
IL1²⁵

Figure 2

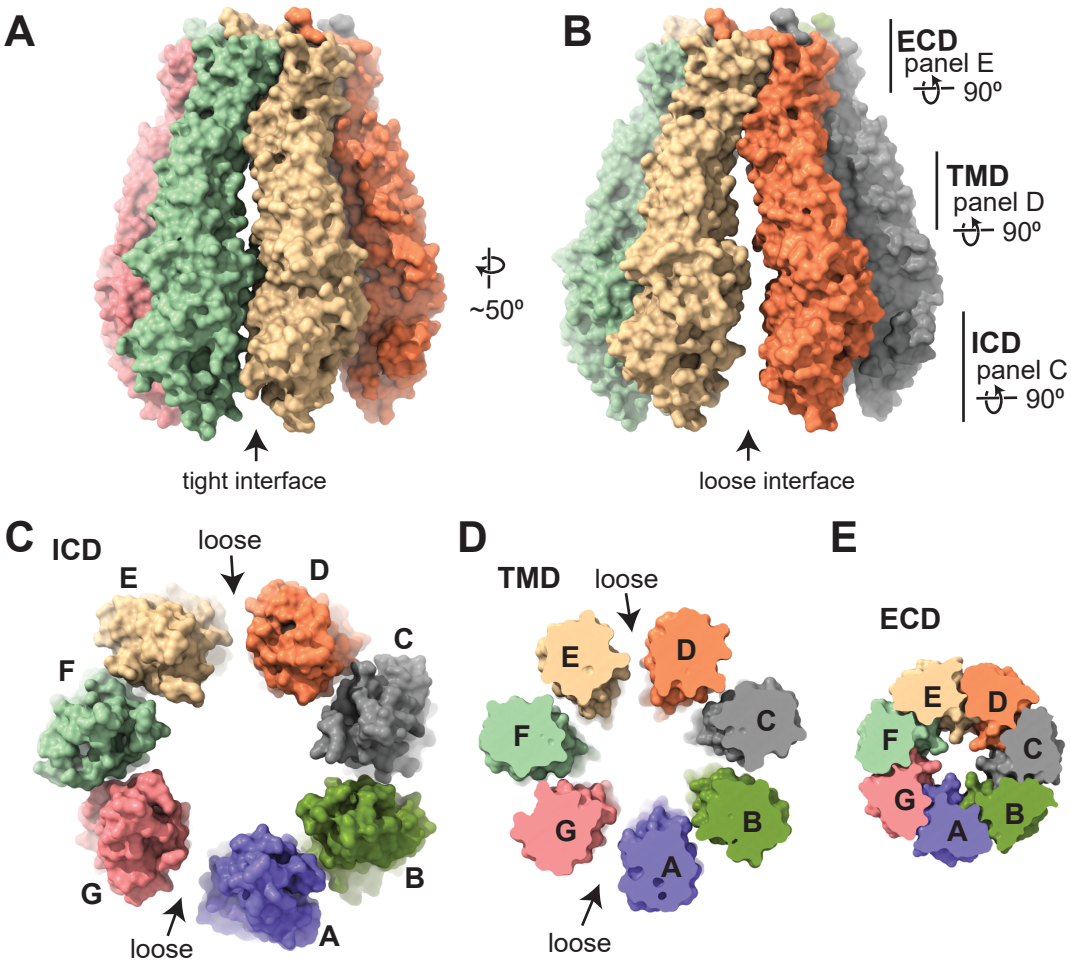
A
B
ECD
panel E
90º
TMD
panel D
90º
ICD
panel C
90º
~50º
tight interface
loose interface
C
ICD
loose
E
D
C
F
G
B
A
loose
D
TMD
loose
E
D
F
C
G
B
A
loose
E
ECD
E
D
F
C
G
A
B

Figure 3

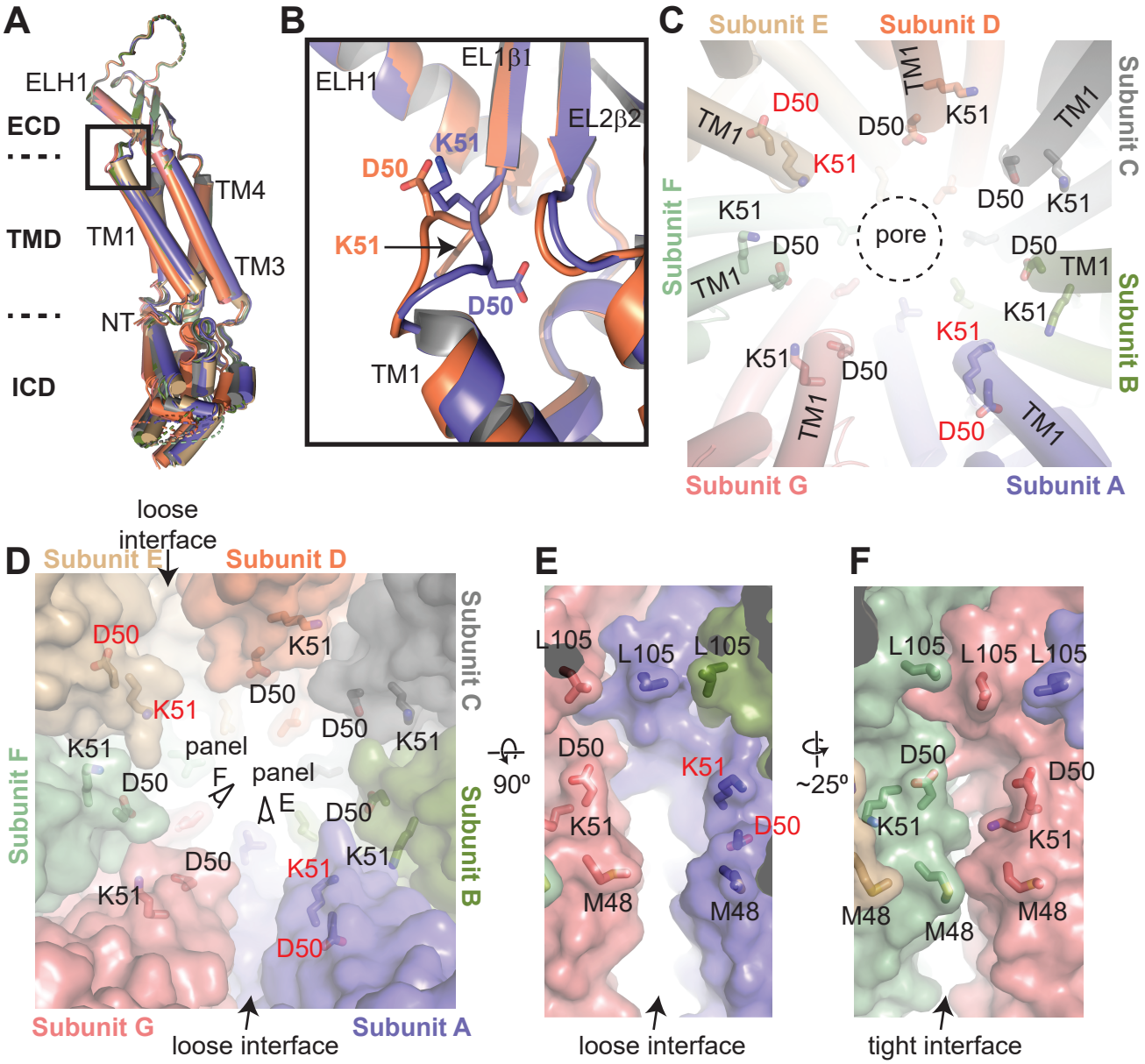
A
ELH1
ECD
TM4
TMD
TM1
TM3
NT
ICD
B
ELH1
EL1β1
EL2β2
K51
D50
K51
D50
TM1
C
Subunit E
Subunit D
Subunit C
Subunit F
Subunit B
Subunit G
Subunit A
pore
D
loose interface
Subunit E
Subunit D
Subunit C
Subunit F
Subunit B
Subunit G
Subunit A
panel F
panel E
90°
loose interface
E
L105
D50
K51
M48
loose interface
~25°
F
L105
D50
K51
M48
tight interface

Figure 4

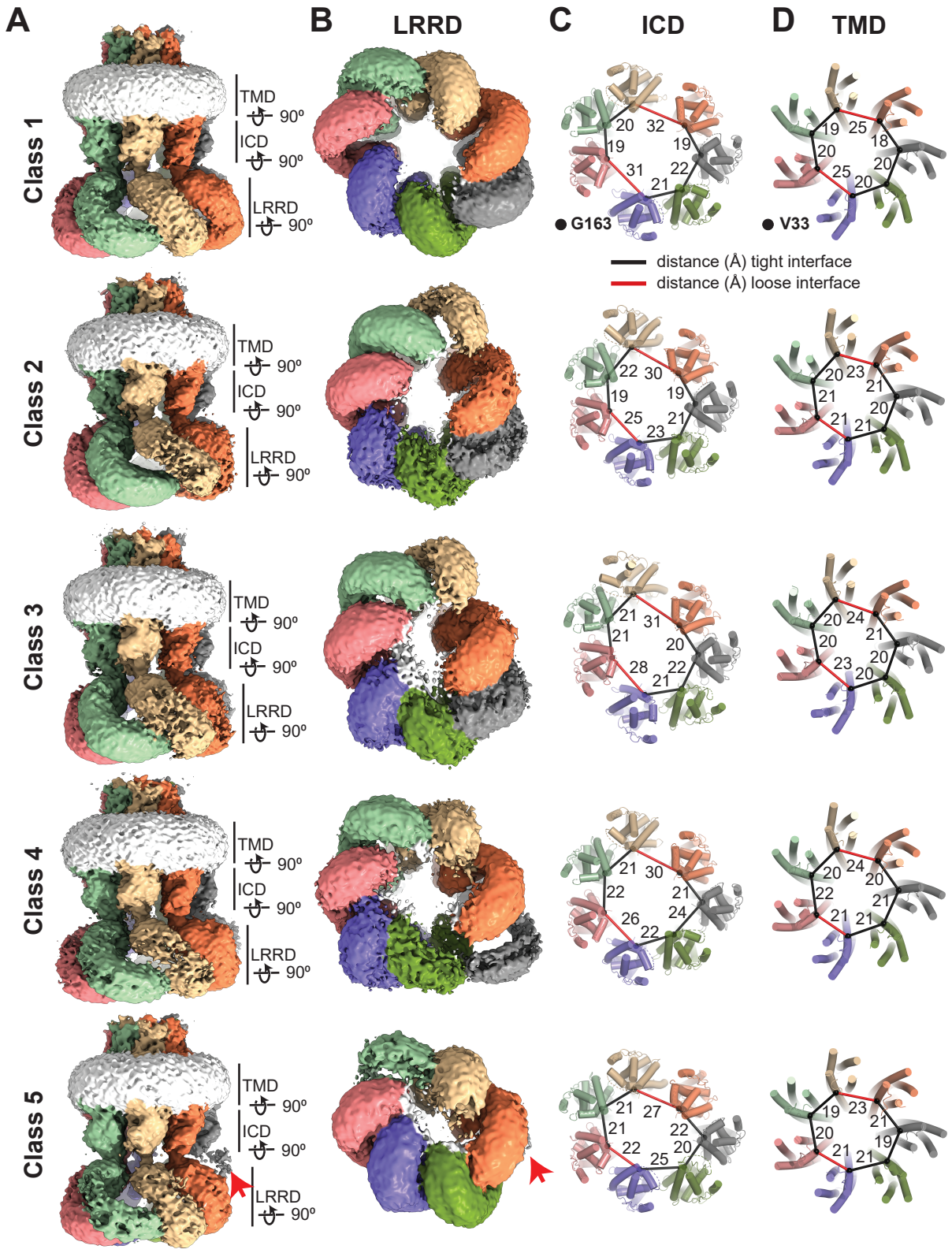
A
B
LRRD
C
ICD
D
TMD
Class 1
Class 2
Class 3
Class 4
Class 5
TMD
90°
ICD
90°
LRRD
90°
G163
V33
distance (Å) tight interface
distance (Å) loose interface

Figure 5

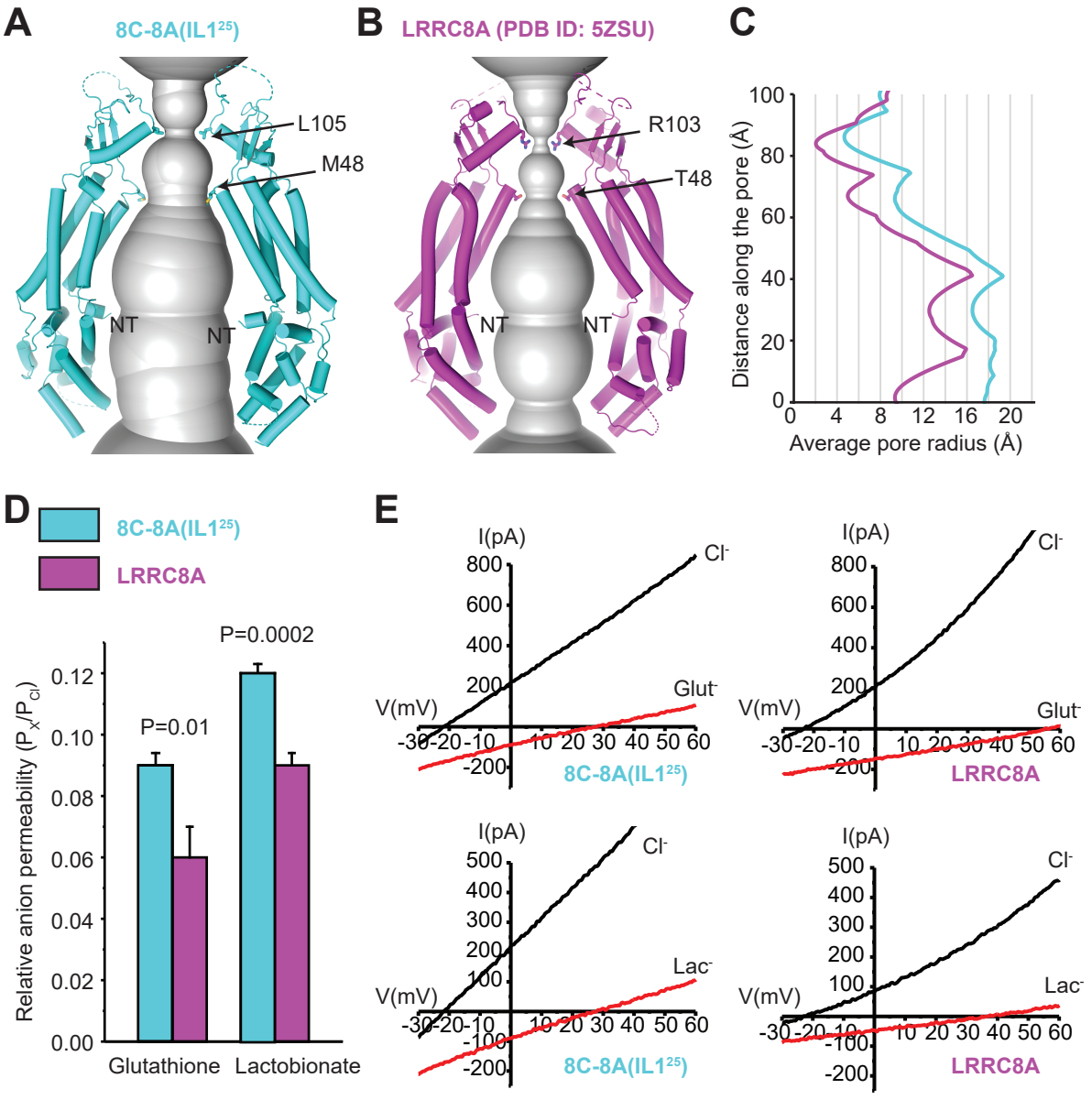
A
8C-8A(IL1²⁵)
L105
M48
NT
NT
B
LRRC8A (PDB ID: 5ZSU)
R103
T48
NT
NT
C
Distance along the pore (Å)
Average pore radius (Å)
D
8C-8A(IL1²⁵)
LRRC8A
P=0.0002
P=0.01
Relative anion permeability (P_X/P_Cl)
Glutathione
Lactobionate
E
I(pA)
V(mV)
Cl-
Glut-
8C-8A(IL1²⁵)
LRRC8A
Lac-

Figure 6

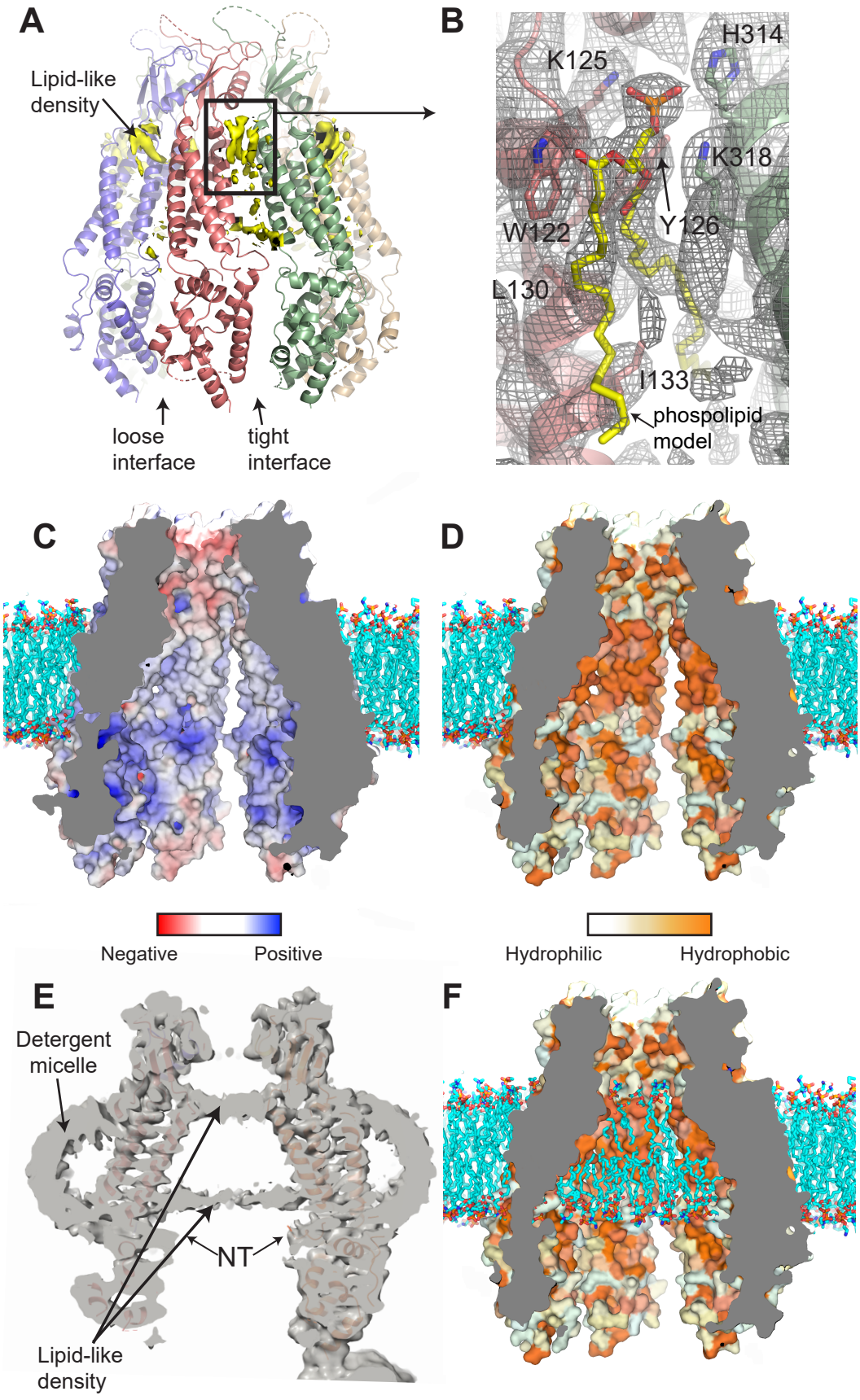
A
Lipid-like density
loose interface
tight interface
B
H314
K125
K318
Y126
W122
L130
I133
phospolipid model
C
Negative
Positive
D
Hydrophilic
Hydrophobic
E
Detergent micelle
NT
Lipid-like density
F

Figure 7

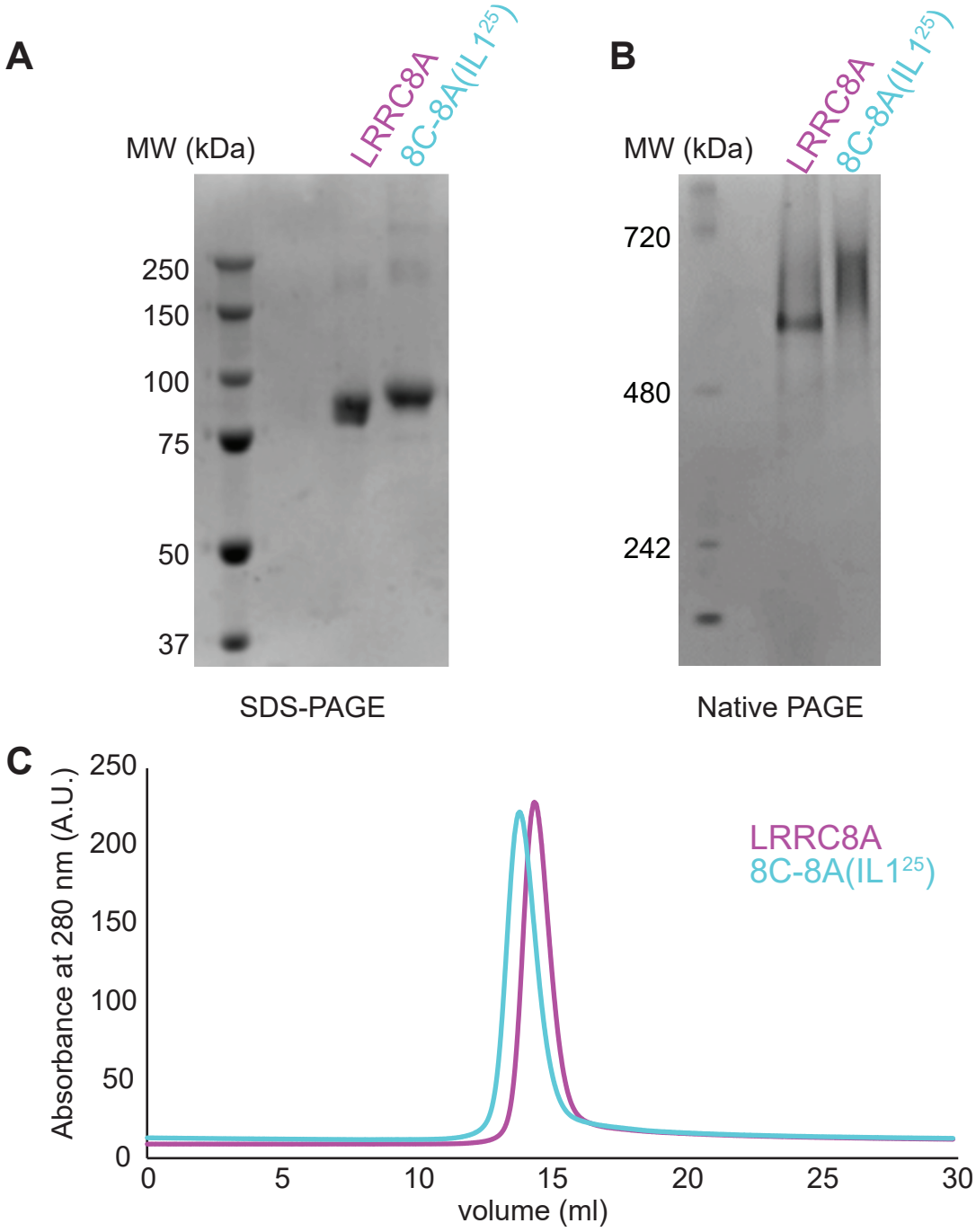

Figure 1 – figure supplement 1

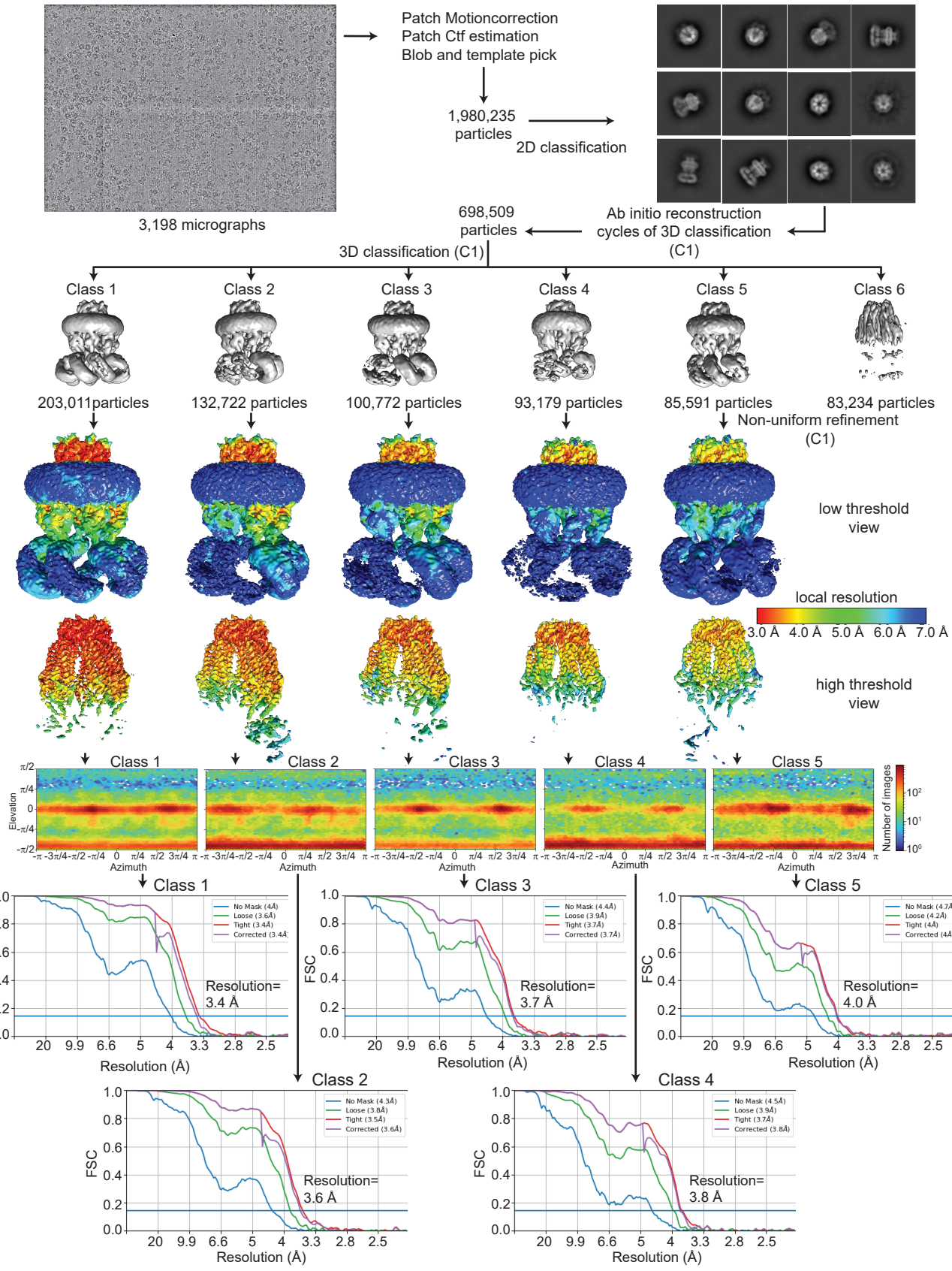

Figure 2 – figure supplement 1

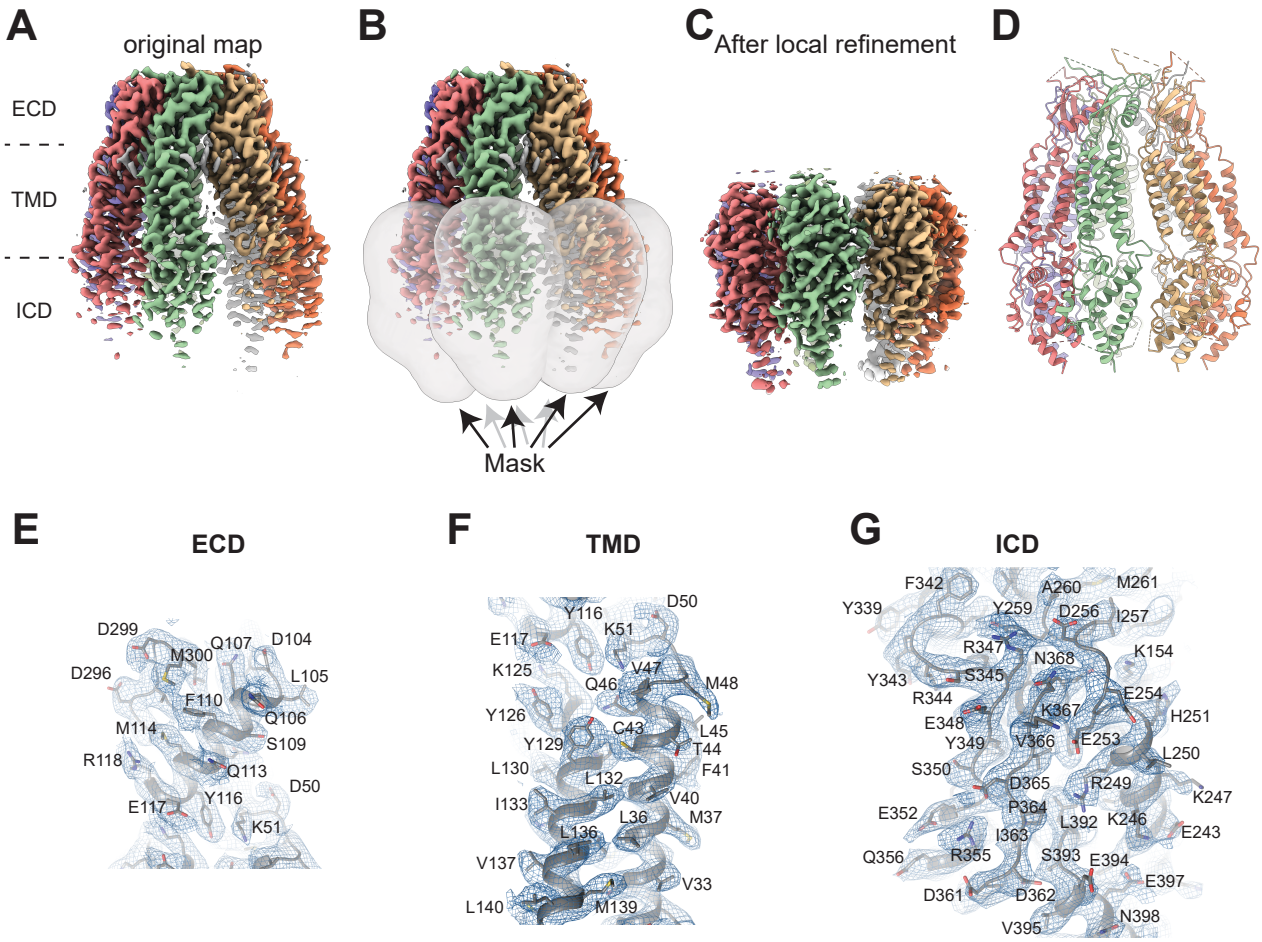

Figure 2 – figure supplement 2

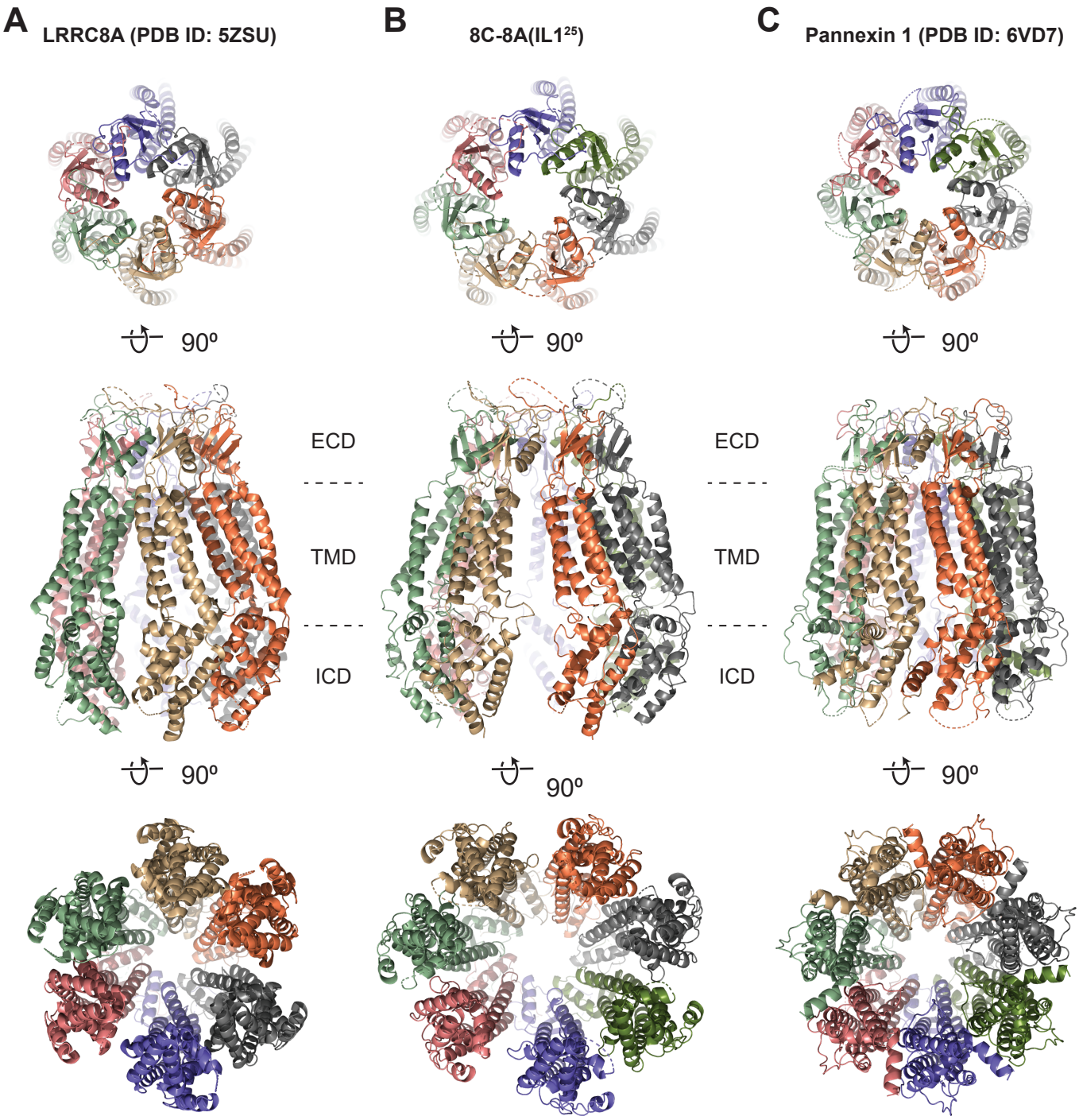

Figure 2 – figure supplement 3

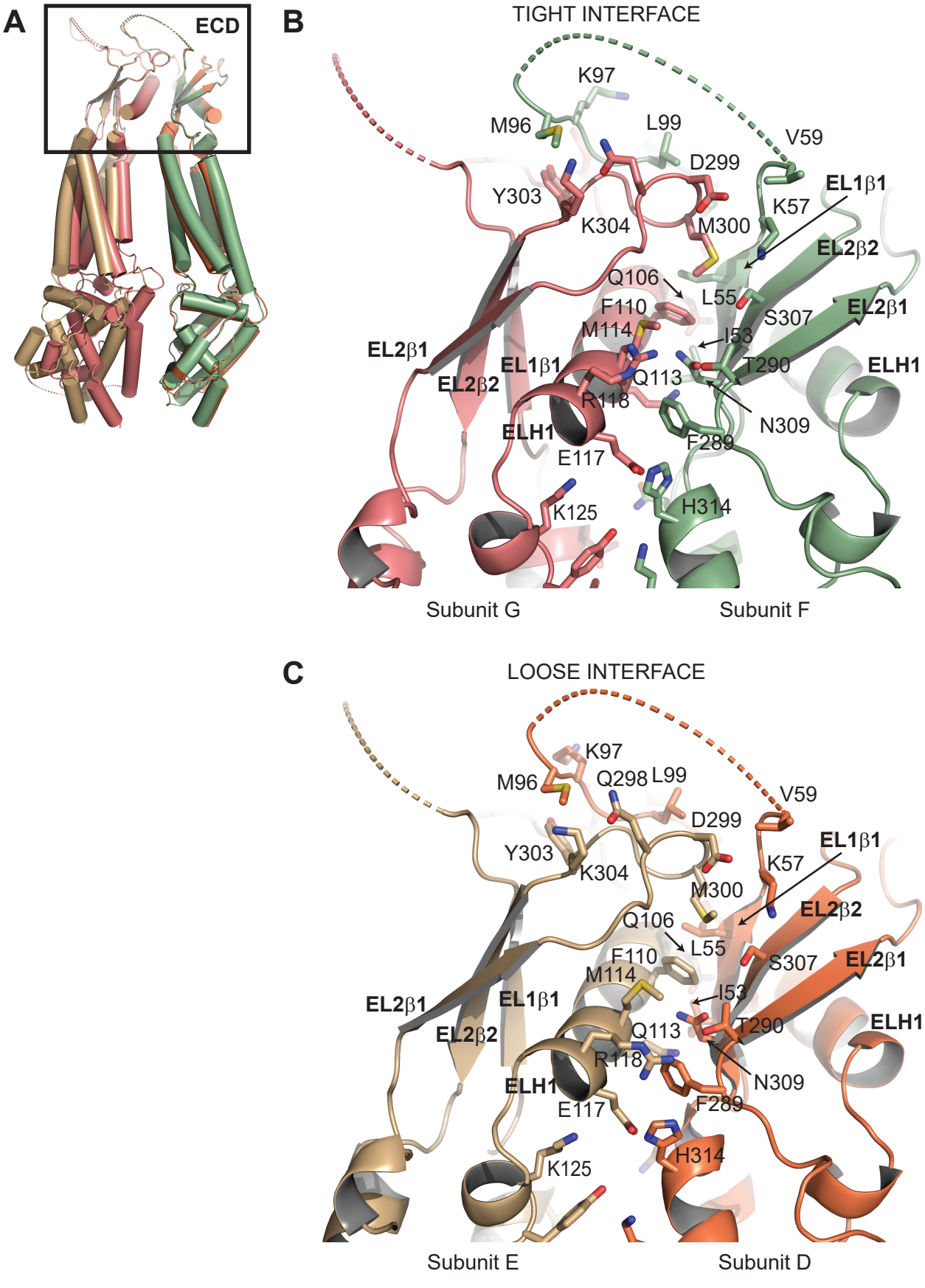

Figure 3 – figure supplement 1

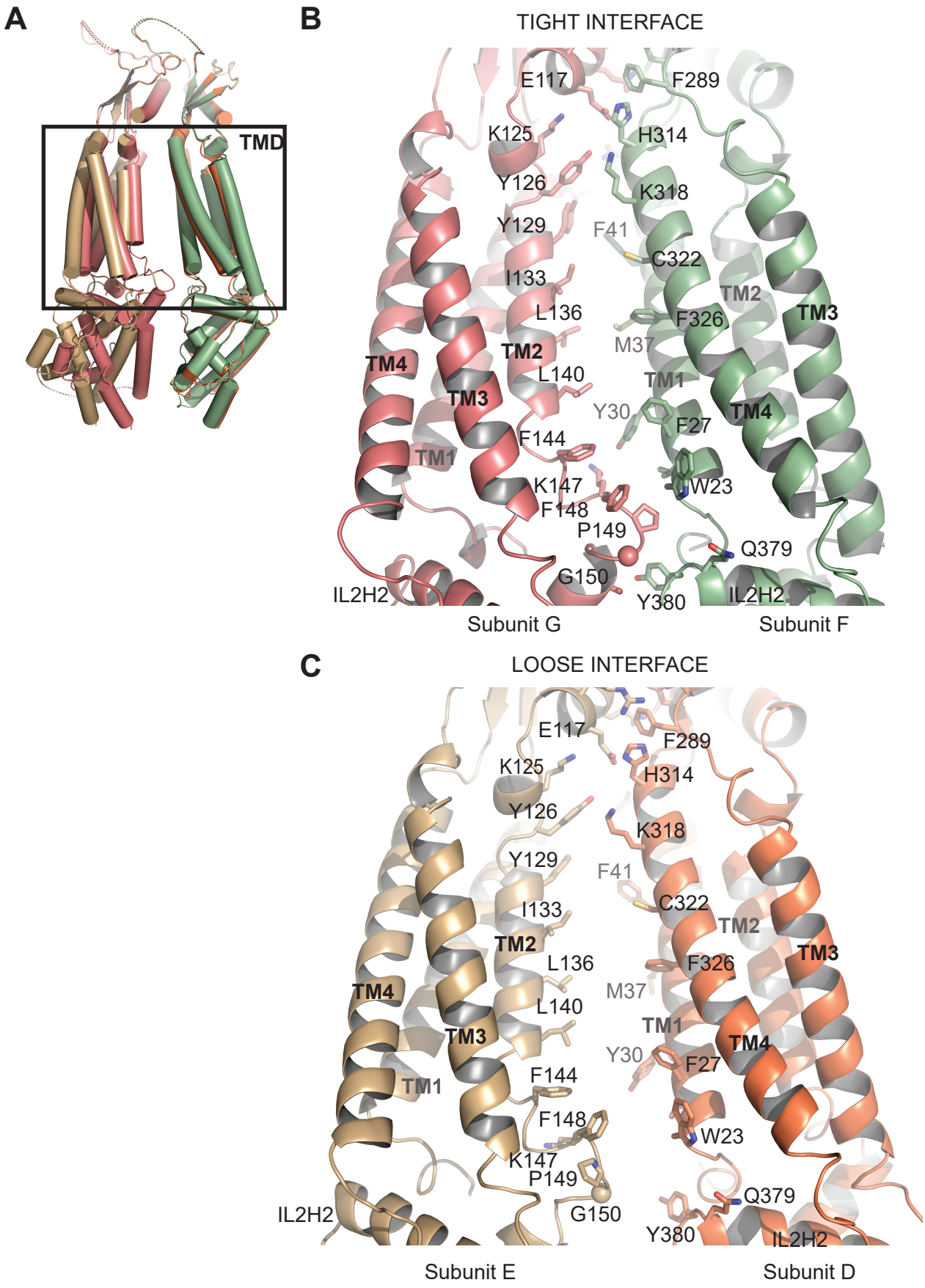

Figure 3 – figure supplement 2

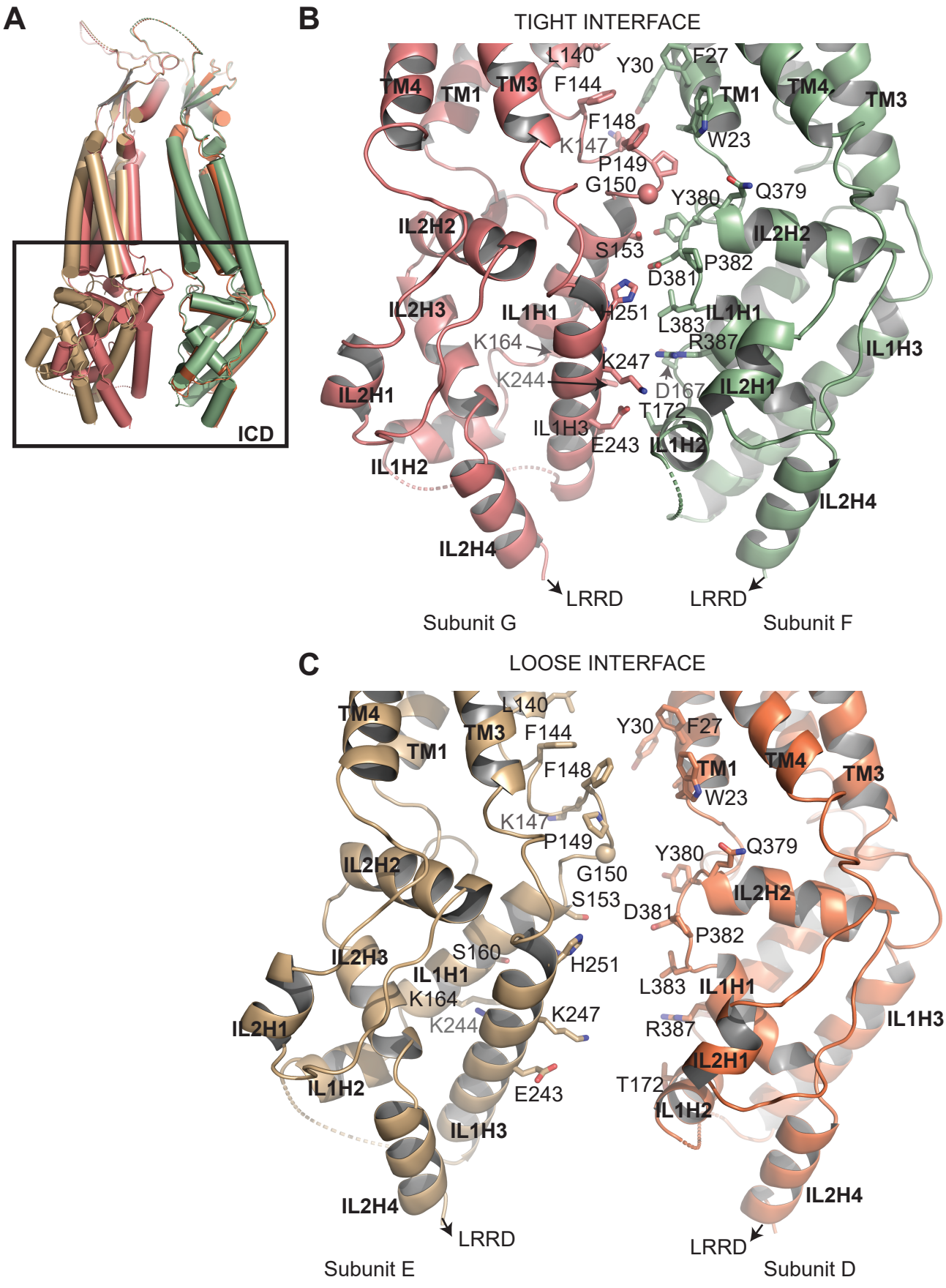

Figure 3 – figure supplement 3

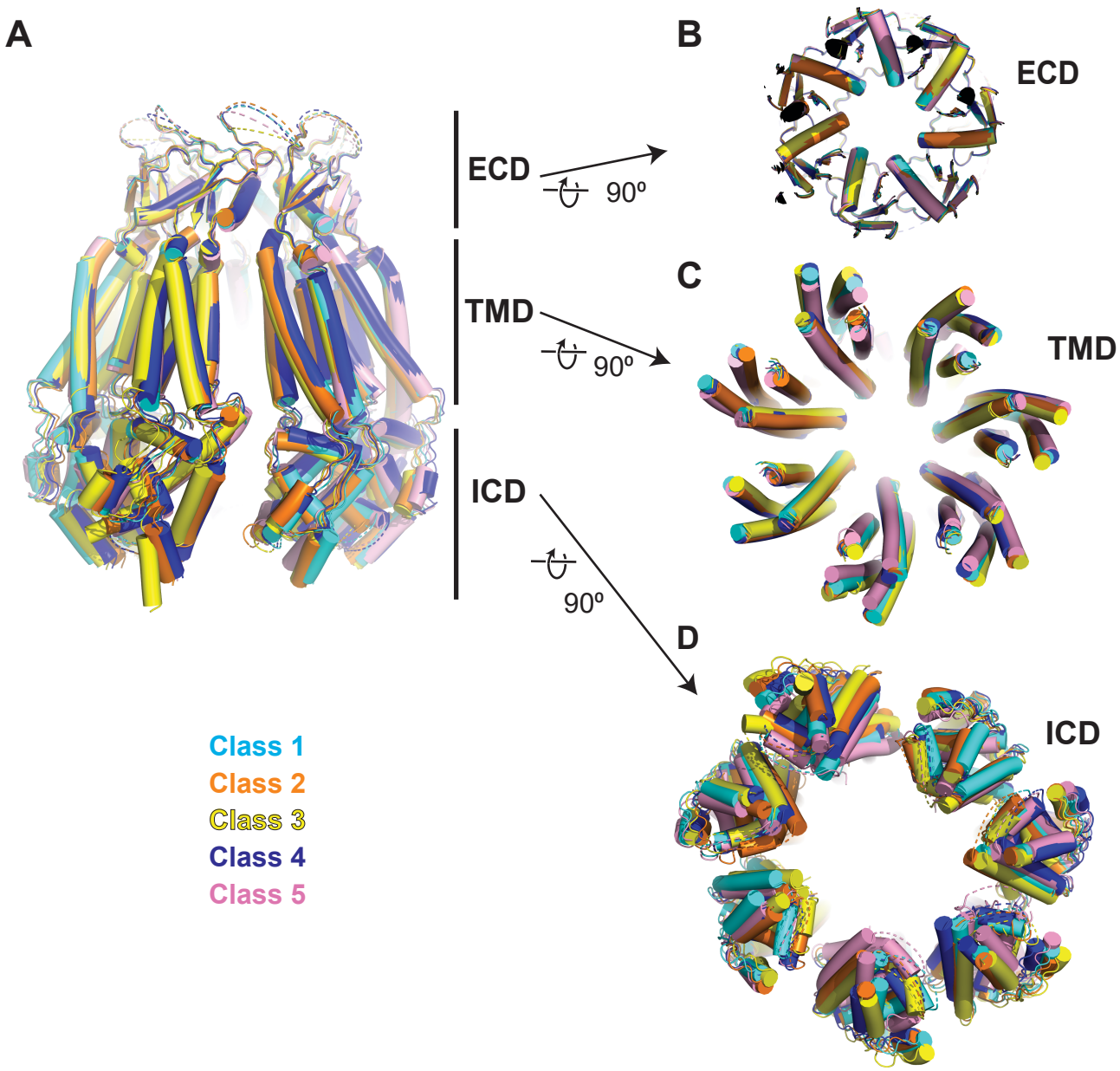

Figure 5 – figure supplement 1

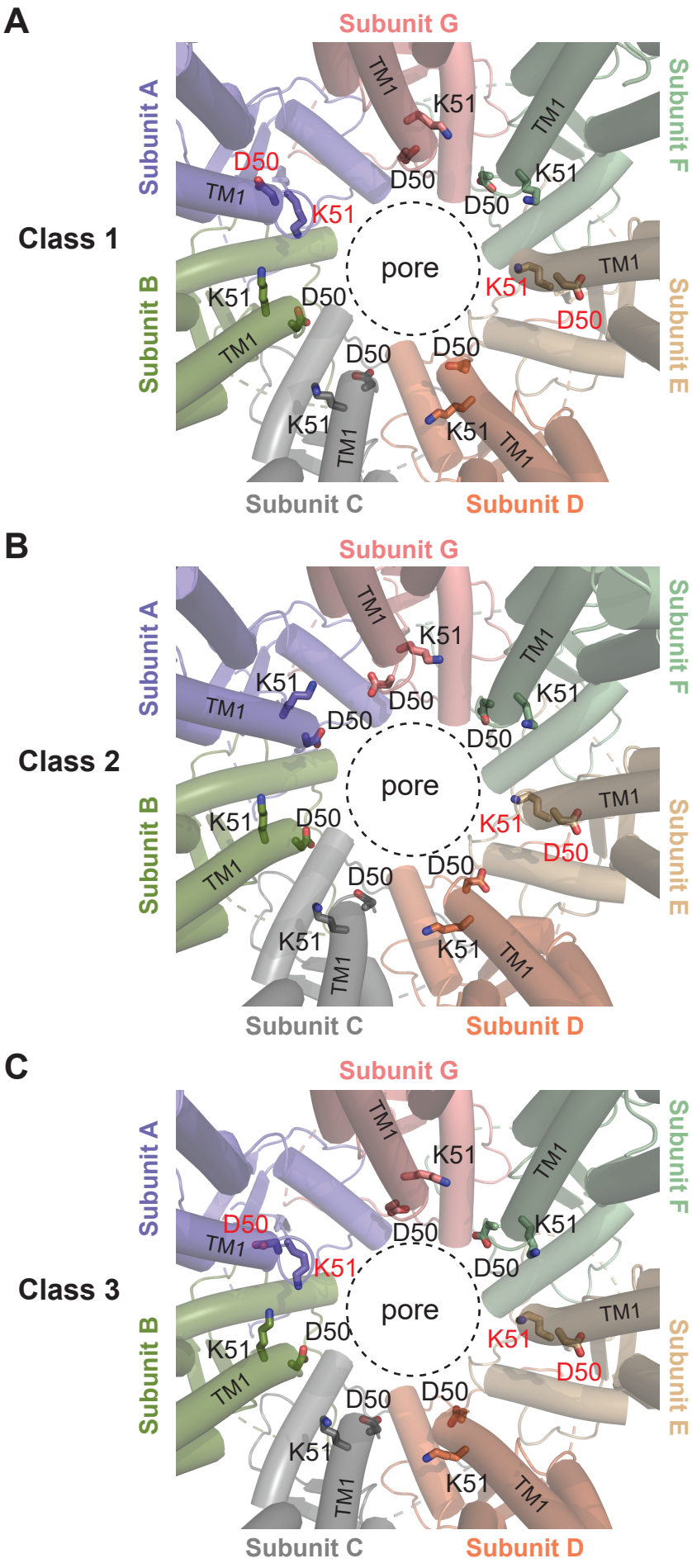

Figure 5 – figure supplement 5

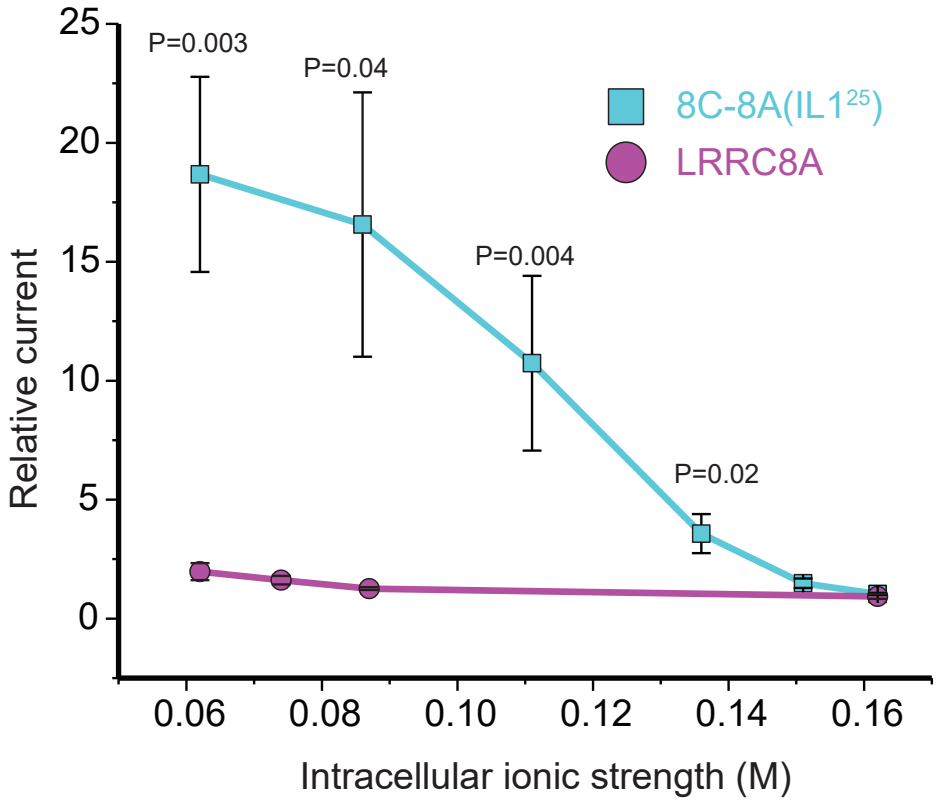

Figure 6 – figure supplement 1

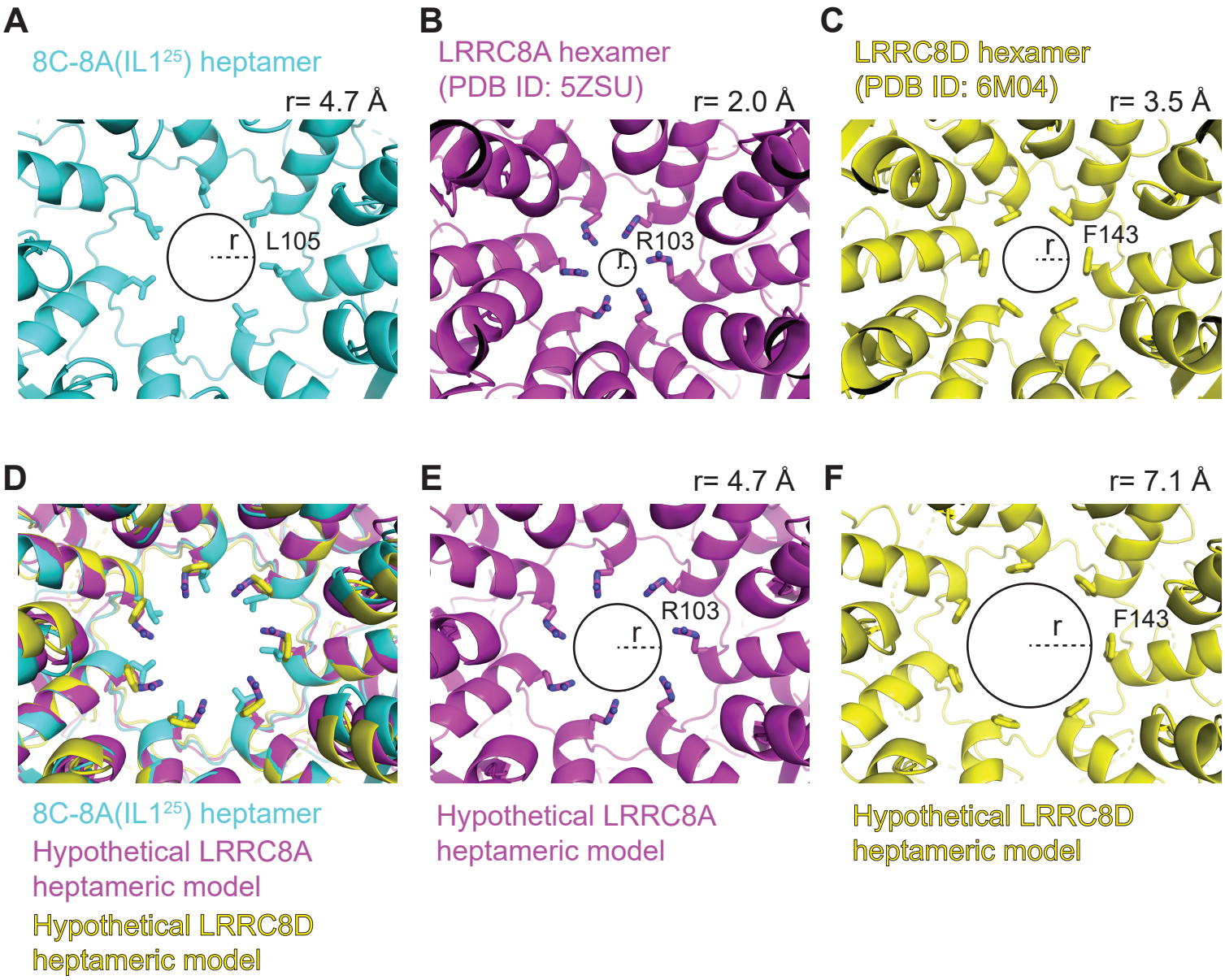

Figure 6 – figure supplement 2

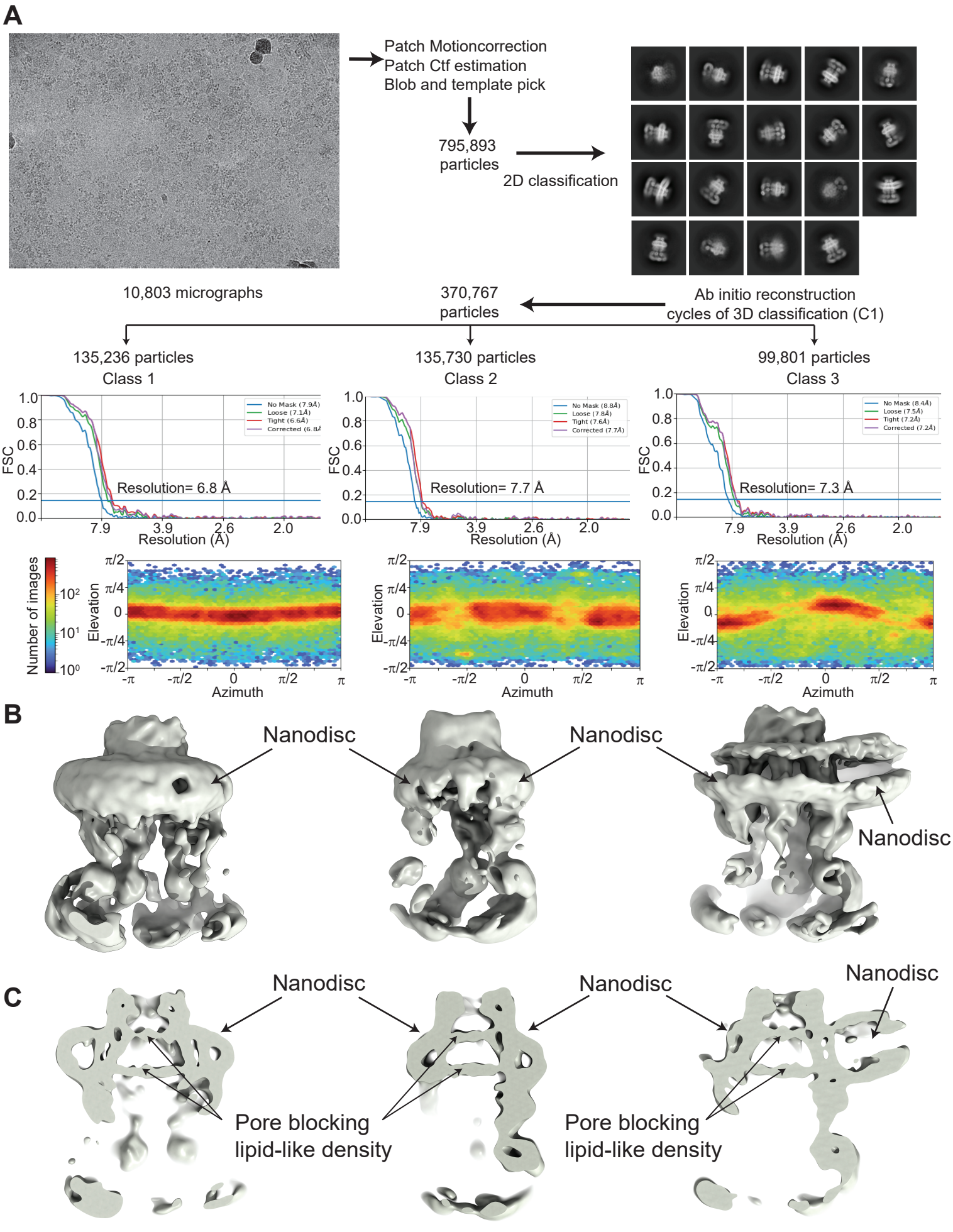

Figure 7 – figure supplement 1